Evaluation of Anti-Erosion Mechanism of 3D Printed Polymer for Various Morphological Arrangements

Author

Muhammad Bilal Khan

(Registration No: 00000361015)

Thesis Supervisor: Dr. Muhammad Rehan Khan

DEPARTMENT OF MECHANICAL ENGINEERING

COLLEGE OF ELECTRICAL & MECHANICAL ENGINEERING

NATIONAL UNIVERSITY OF SCIENCES AND TECHNOLOGY

ISLAMABAD, PAKISTAN

(2024)

THESIS ACCEPTANCE CERTIFICATE

I Certified that final copy of MS/MPhil thesis written by Ms. **NS Muhammad Bilal Khan**, Registration No. **00000361015** of **NUST College of E&ME** has been vetted by undersigned, found complete in all respects as per NUST Statutes/Regulations, is free of plagiarism, errors, and mistakes and is accepted as partial fulfillment for award of MS/MPhil degree. It is further certified that necessary amendments as pointed out by GEC members of the scholar have also been incorporated in the said thesis.

Signature: _____
Name of Supervisor: **Dr. Muhammad Rehan Khan**

Date: 21-3-2024

Signature (HOD): _____
Name: **Dr. Imran Akhtar**
Date: 21-3-2024

Signature (Dean): _____
Name: **Dr. Nasir Rashid**
Dated: 21-3-2024

Dedicated to my exceptional parents and beloved siblings, whose tremendous support and cooperation have been instrumental in guiding me towards this wonderful achievement.

ACKNOWLEDGEMENTS

I would like to begin by expressing my deepest gratitude to Allah for granting me the strength, perseverance, and guidance throughout my academic journey, including the completion of my MS thesis. I am truly thankful for His blessings and mercy, which have enabled me to achieve this milestone.

I would also like to extend my heartfelt thanks to my parents for their unwavering support, love, and encouragement. Their belief in me has been a constant source of strength and motivation.

Additionally, I am deeply thankful to my supervisor, Dr. Muhammad Rehan Khan, for his invaluable guidance, support, and mentorship during the completion of my MS thesis. His expertise and patience have been instrumental in shaping this work.

ABSTRACT

Erosive wear in pipelines is a persistent challenge in the hydrocarbon and mineral processing industry. Erosion is a significant contributor to the failure of fluid-handling equipment, such as pumps and pipes. Therefore, the material losses occurring in slurry flow need to be studied and understood to develop protective guidelines for oil and gas production equipment. This study examined the effect of slurry on Polylactic Acid (PLA) subjected to Fused Deposition Modeling (FDM) using various morphologies. The investigated variables included design, concentration, and impact angle, with the utilization of Taguchi design in the experimental setup. Experiments were conducted employing a slurry jet testing apparatus, with three different designs D1 (Flat), D2 (Groove), and D3 (Square groove). The slurry concentrations were maintained at 1%, 3%, and 5% by weight, and the striking angles (IA) were set at 60°, 75°, and 90°. A scanning electron microscope (SEM) was employed to examine the eroded surfaces. Results indicated the development of cracks, micro-cutting, flakes, and craters on the facade of the eroded region. The findings also reveal that D2 outperforms both D1 and D2 in terms of erosion resistance. An ANOVA test was performed, revealing that the thickness loss of PLA is significantly influenced by concentration and design the results suggest significant influences from each factor on the response, with concentration (64.68%) standing out as the primary contributor, followed by design (23.80%) and Impact Angle (IA) (10.56%) for liquid-sand flow similarly concentration contributing 50.49%, design 38.85% and impact angle 10.00% for liquid-sand-gas flow

Keywords: Erosive wear; 3D printing; Regression; Polylactic acid

TABLE OF CONTENTS

LIST OF TABLES

LIST OF FIGURES

LIST OF ABBREVIATIONS

PLA	Poly-Lactic Acid
ANOVA	Analysis Of Variance
RSM	Response Surface Methodology
2D	2 Dimensional
3D	3 Dimensional
ABS	Acrylonitrile Butadiene Styrene
SEM	Scanning Electron Microscopy
S/N ratio	Signal to Noise ratio
FDM	Fused Deposition Modelling

CHAPTER 1 : INTRODUCTION

1.1 Background of Study:

Erosion caused by sand particles is a primary method of material removal and is commonly observed in the petroleum and mineral processing industry. Damage from erosive wear occurs when sand particles carried by the fluid impact the internal surface of pipelines [1]. Erosion can lead to substantial harm to piping networks within the petroleum production industry, resulting in machinery malfunctions and the need for replacing production equipment. To mitigate pipeline erosion, a considerable amount is spent annually on maintaining and replacing damaged piping components. Failure to detect erosion-induced damage could lead to equipment malfunctions, changes in flow, and jeopardize the overall operational safety of the process [2].

A significant issue in the petroleum extraction and mineral processing industry is the presence of fine sand particles. Fines, typically defined as sand particles smaller than 62 microns, can cause erosive impacts on pipelines. These particles impact the safety of operations, decrease the efficiency of production processes, and cause significant damage to flow devices, shortening their lifespan. The interaction between particles and the pipeline walls is the primary reason for the deterioration of the pipe wall. Previous studies have focused on understanding the damage caused by erosion from sand particles and the factors that influence erosion, such as the properties of the target wall, characteristics of the carrier fluid, and properties of the erodent [3], [4], [5].

Additionally, erosive wear in a single-phase flow with fine particles of sand suspended in the carrier fluid is a complicated experience. The perplexity of erosive wear becomes even more pronounced in multiphase flow with fine particles of sand in the fluid carrier due to various multiphase flow patterns. Among the many factors influencing erosion, particle concentration is recognized as the predominant. The Limited comprehension of particle concentration and its effect on the erosive wear process poses a challenge in analyzing the erosive wear mechanism. Therefore, gaining an optimal insight of particle concentration is crucial for comprehending the multiphase erosive wear process. Most existing erosive wear data are derived from direct impact tests and are based on a single-phase gas or liquid carrier fluid. The accuracy of the direct impact test is bounded by single-phase flow conditions and flat target surfaces. Managing the complexities tied to a multiphase erosion problem and to quantify erosion distribution and erosion rate under conditions

closer to field operating conditions, there is a need to develop experiments that can provide quantitative and qualitative measurements of erosion-induced damage for multiphase flow conditions.

Prior research on erosive wear has focused on various ductile materials such as carbon steel, nickel, and aluminum alloys, providing valuable insights into the phenomenon under multiphase flow. However, there is a noticeable research gap in understanding erosive wear in polymers. Polymers, exemplified by Polylactic Acid (PLA), derived from sugarcane fermentation, possess unique attributes such as biocompatibility and biodegradability. This study aims to fill the research gap by investigating the erosive wear behavior of PLA. By focusing on PLA as the material of interest, we aim to examine the complex interaction between erosive wear and different pH environments, providing valuable insights into the erosive behavior of polymers compared to traditional ductile materials. The biocompatible and biodegradable nature of PLA increases its relevance in current research and applications, emphasizing the importance of studying erosive wear in this category of materials.

1.2 Problem Statement:

In the hydrocarbon industry, the production fluids often carry sand fines along with them. These production fluids may consist of gas and liquid phases, resulting in the formation of multiphase flow patterns. Pipeline multiphase flow refers to the simultaneous passage of two or more phases via a pipe at different flow regimes. Phases such as solids, liquids, and gases can all exist in a multiphase flow. Due to the phases' varying configurations, comprehending the properties of multiphase flow is more difficult than that of single-phase flow. Sand movement in liquid and gas phases is frequently reported to follow the slug flow regime. Gas bubbles occupy the upper part of the pipe and are separated from the continuous liquid phase in the lower half of the horizontally oriented pipe due to the difference in carrier phase densities. Liquid slugs segregated by portions of the gaseous phase may occupy the intact pipe cross-sectional area. Because only the liquid phase is used to convey the erodent’s and the slug body has the maximum liquid holdup, the slug body is the main source of erosion in the erosive slug flow pattern. In pipelines, erosion and corrosion damage are caused by entrained sand, which mostly moves in the slug body's liquid. The presence of two carrier fluid phases with sand transported through a pipe exacerbates erosion-corrosion. The propagation of erosion-corrosion depends on the flow patterns, velocity, impact angle, erodent properties, and chemical properties of the pipeline material. When sand is present simultaneously with air and water, continuous impingements of the sand enhance the corrosion process. To

regulate and reduce the production of sand, gravel packs, sand screens, or sand elimination are placed at the entrance of key production lines. Nevertheless, in the mineral and hydrocarbon processing sectors, small particles (less than 62.5 μm) cannot be kept out of the fluid phase by using a typical sand screen. These sand fines could go past sand filters and seriously harm pipe systems due to erosion. In the hydrocarbon production sector, erosion can seriously harm pipe networks, resulting in equipment failure and the need to replace production machinery.

While numerous studies have been conducted on various parameters affecting erosion, there remain certain factors that have not been thoroughly examined. In addressing the challenges posed by erosion, this research focuses on investigating an alternative material, Poly-Lactic Acid (PLA), considering various morphologies, concentrations, and impingement angles. The overarching objective of this research is to devise distinct designs through 3D printing of PLA to enhance the material's resistance to erosion.

1.3 Objectives

This research seeks to advance the understanding of the erosion behavior of PLA in both single-phase (water-sand) and multiphase (air-water-sand) flow conditions under erosion circumstances. This will be accomplished through the following objectives:

- To assess anti-erosion behavior of 3D printed PLA with various morphological arrangement for liquid-sand flow conditions.
- To assess anti-erosion behavior of 3D printed PLA for Multi-phase(liquid-sand-air) flow conditions.

1.4 Scope of the study:

This research seeks to comprehensively assess the effects of various morphological variations on Polylactic Acid (PLA), aiming to provide valuable insights into its erosive mechanisms. The findings of this investigation have the potential to enhance researchers' understanding of how PLA responds to different morphologies, which is essential for optimizing materials and developing more resilient PLA-based products. To assess the erosive wear mechanism of the 3D printed PLA, a direct impact experimental apparatus was utilized. The study involved the selection of different sand concentration levels (1 wt.%, 3 wt.%, and 5 wt.%) to evaluate erosion performance in both liquid sand flow and liquid sand air flow conditions. Additionally, three different angles (60°, 75°,

and 90°) were used in this research. Furthermore, three distinct designs (D1 Flat, D2 groove, and D3 square groove) were considered for evaluation.

1.5 Outline of thesis:

This research consists of 5 chapters. Chapter 1 outlines the Background of study, problem statement, objectives, scope of the study. Chapter 2 includes a comprehensive examination of erosion mechanisms in different ductile materials, exploring various flow patterns and reviewing experimental methodologies from previous studies on erosive wear in both ductile materials and polymers. Chapter 3 outlines the research methodology. Chapter 4 thoroughly discusses qualitative and quantitative results, providing a detailed analysis of erosive wear and material performance under different conditions. Chapter 5 serves as the conclusion, summarizing key findings and presenting future research recommendations for further exploration in this field.

CHAPTER 2 : LITRATURE REVIEW

2.1 Introduction:

The primary focus of this research was to comprehend the physical process of sand fines erosive wear on metal surfaces by assessing the factors influencing erosive wear. Moreover, the study aims to assess the impact of different morphologies on the target material and the resulting damage caused by erodent particles and concentration. While prior research has examined erosion on different metallic target materials, there is a noticeable gap in understanding trends related to PLA erosion.

Comprehending the erosive wear phenomenon in multiphase flow requires an awareness and comprehension of multiple ideas. First and foremost, it is crucial to have a thorough understanding of the mechanism of solid particle erosion in both single-phase and multiphase flow. Impact velocity, impingement angle, wall material, particle shape, size, density, carrier fluid characteristics (density, viscosity), and carrier fluid velocity are the main elements affecting erosive wear. It is essential to comprehend multiphase flow and the dispersion of erodent solid particles in various phases. Particle impact velocities can be determined from the velocities of the respective gas and liquid phases. The concentration of solid particles entrained in the carrier phases is another important element. The entrained particles in the carrier phases of a multiphase flow will have velocities that match those of the corresponding carrier phases. Finally, it is crucial to comprehend how the particles affect the geometry of the wall and remove the wall material to compute the erosion brought on by solid particles. These elements and how they affect erosion are covered in more detail in the next sections of this chapter.

2.2 Mechanism of erosive wear

Erosive wear is a complex process, involving multiple simultaneous mechanisms that interact with each other. This simultaneous occurrence of various mechanisms makes erosive wear a challenging and ambiguous phenomenon. The combined impact and integrated outcome of these mechanisms contribute to the overall material degradation rate [6]. Evaluating the precision and accuracy in microscopic approaches is crucial for obtaining useful data from experimental results. It is evident from the literature that the erosive wear mechanism differs for ductile and brittle materials [7], [8].

Finnie [9] and Bitter [10] examined the erosive wear mechanism in ductile materials, revealing that cutting emerges as the predominant erosion mechanism during oblique impacts, attributed to rodent impact. Their findings also indicated that brittle materials undergo degradation through the development of subsurface cracks, a consequence of erodent impact on target surfaces. Figure 2.1 presents the erosive wear mechanisms observed in both ductile and brittle materials.

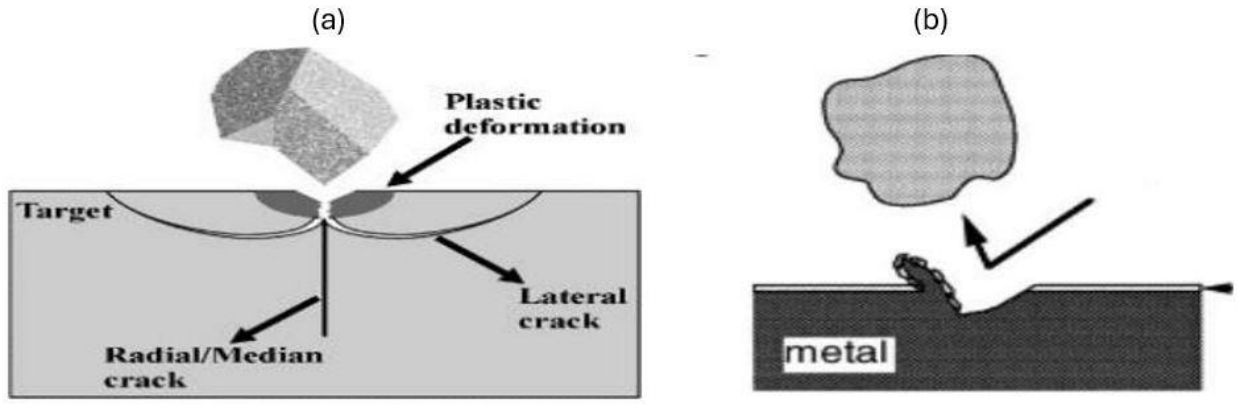

Figure 2.1: Mechanism of Solid Particles Erosion (a) Ductile Material (b) Brittle Material [11]

Finnie's [12] investigated, the investigation of erosive wear mechanisms revealed that at a low impact angle, particles create a crater on the target surface before moving away. The sand particles that come before remove the previously formed chip, while particles hitting the target surface at a higher impingement angle hinder the surface-cutting process. This research is specifically focused on predicting erosive wear caused by erodent at low-impact angles.

Bitter [10] introduced a model based on wear mechanisms and deformation to study erosive wear caused by erodent at a higher impact angle. Figure 2.2 presents the erosive wear mechanism for both ductile and brittle materials.

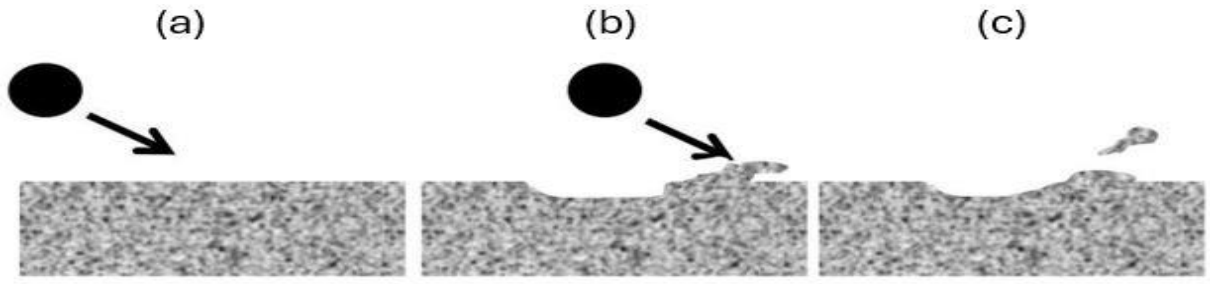

Figure 2.2: Schematic of Erosive wear Mechanism in Ductile Materials (a) Before erodent's impact (b) Crater formation and piling materials at one side of the crater (c) Material separation from the surface [13]

2.3 Influential Parameters of Sediment Erosion

As previously mentioned, sediment erosion in the Pelton bucket is a complicated phenomenon that is not fully interpreted. This phenomenon is influenced by various parameters, as depicted in fig. 2.3.

Figure 2.3: Influential Parameters of Erosion [14]

Some of these parameters are of great importance and significantly impact the rate and mechanism of erosive wear. A comprehensive examination of these parameters is provided below.

2.3.1 Influence of Characteristics and Types of Sediments on Erosion

The extent of sediment erosion is directly tied to the hardness of the particles causing erosion, regardless of their size. Likewise, erosion intensity fluctuates with the size of the sediment particles. Typically, particles exceeding 0.2-0.25 mm led to notable erosive wear in pipes. Conversely, fine particles result in comparatively milder erosion at lower operating heads but more severe erosion at higher operating heads in pipes and fittings. Erosion rates also vary depending on the shape of sediment particles, with research suggesting that sharp and angular shapes induce more erosion than round shapes [15].

2.3.2 Influence of flow velocity on erosion

Finnie[12] investigated that the velocity of the erodent directly affects both the erosion rate and mechanism. He established a relationship between erosion rate (ER) and erodent impact velocity (V_p) as follows:

$$ER \propto \left(V_p\right)^n \qquad 2.1$$

In this equation, n is a constant ranging from 2 to 2.4. Subsequently, Finnie discovered that considering the rotation of the erodent introduces an additional term dependent on the cubic velocity exponent.

In a more recent study, Oka, and Yoshida [16] conducted numerous erosion tests using a sand erodent. They determined that the computed value of n ranged from 1.6 to 2.6, depending on the material hardness.

2.3.3 Influence of sand particle size on erosion

The key factors influencing the material removal rate in erosion processes are primarily the size, angularity, and hardness of the erodent. Numerous studies, such as those referenced in [17], [18], [19] have attempted to untangle the relationship between erodent characteristics and material removal, yet a comprehensive understanding of the degradation mechanism has not been achieved. In a study by Levy et al. [20] the impact of erodent hardness on material removal in ductile metals was examined for five different erodent types. Their findings suggested that soft erodent's like calcite and apatite exhibit a low erosive wear rate due to the breakage of weak particles upon impact, while the erosion rate remains constant for particles with a Vickers hardness value of 700 HV, as higher hardness particles do not shatter upon impact.

Arabnejad et al. [21] observed that, for harder target metals like stainless steel, Si C erodent causes more erosion compared to SiO2. Figure 2.4 illustrates that when erodent hardness is lower than the impact surface hardness, there is not a substantial increase in material removal. Conversely, the erodent maintains its integrity during impact when it has higher hardness levels than the target material. Lin et al. [22] explored the correlation between the erosion of stainless steel and the sizes of erodent particles using a direct impact test. The erosive wear test revealed that the erosion ratio increases with the growth of erodent size, but 75 μm sand erodent, despite being smaller, degrades

more material, as shown in Figure 2.5. It was also noted that even though the 75 µm sand erodent is smaller, its sharpness is higher, resulting in significant erosion on the specimen surface.

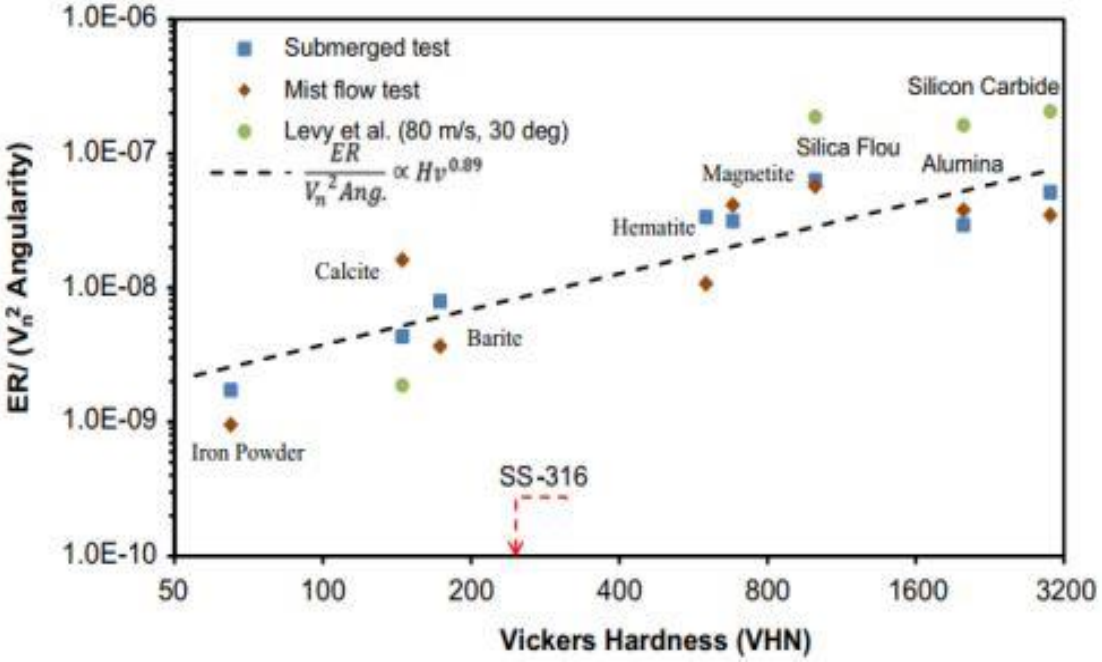

Figure 2.4: Correlation between normalized erosion and particle hardness [21]

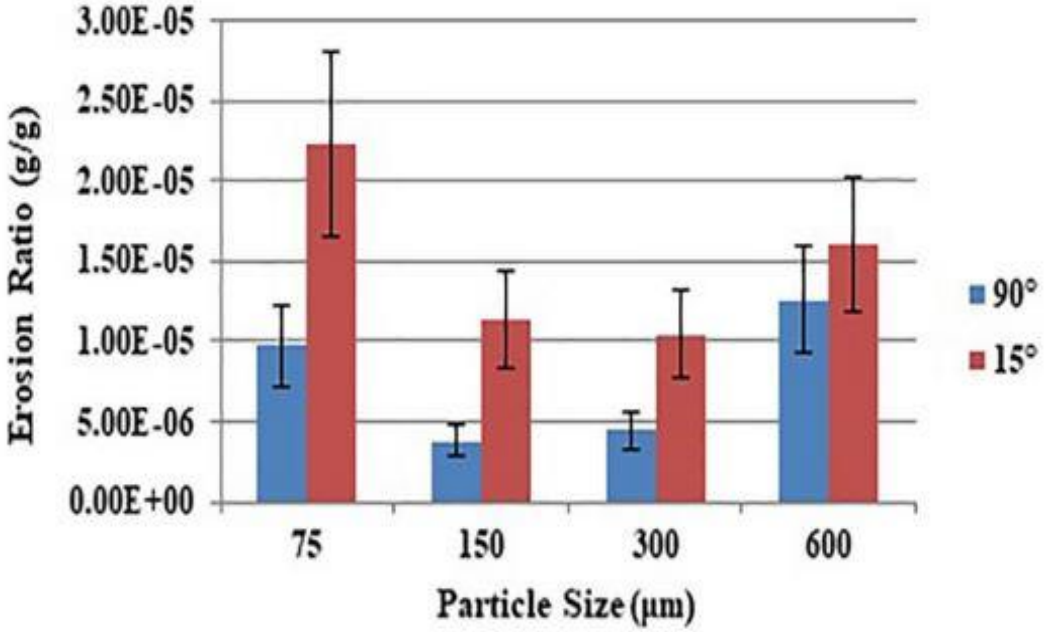

Figure 2.5: Erosion test results for different particle sizes [22]

2.3.4 Influence of Sand Particles Concentration on Erosion

By changing the concentration of erodent particles there is a corresponding rise in the number of particles contacting the chosen material. Consequently, this heightened particle impact results in an accelerated erosion rate. In research carried by Rajahram et al. [23] in 2011, the concentration of sand particles was systematically increased from 1% to 5%. The observed trend indicated that as the concentration of sand particles increased, so did the erosive wear rate. This can be associated to the amplified impact of a bigger number of sand particles on the surface of the target material, leading to an enhanced erosion effect, as shown in Figure 2.6

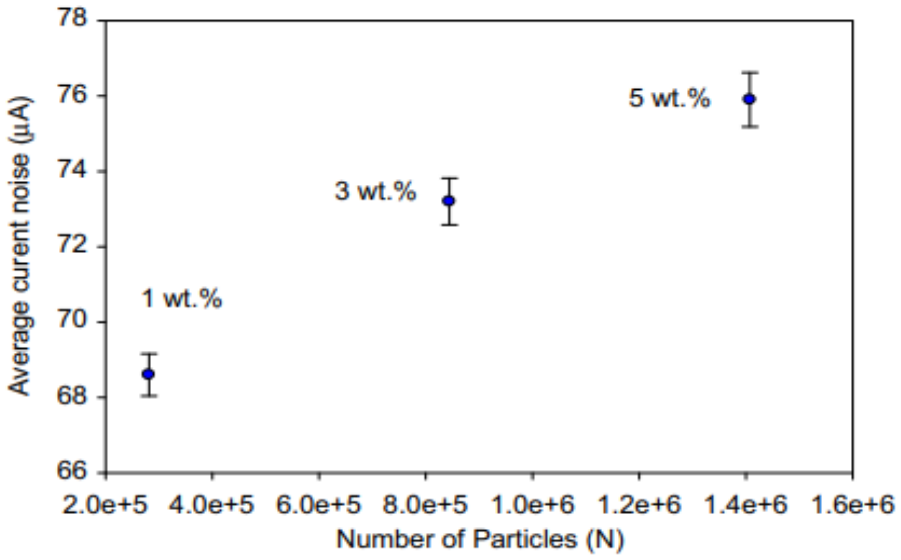

Figure 2.6: Variation of erosive wear rate with increased particle concentration depicted in form of current noise ratio [24]

2.3.5 Influence of Nozzle Diameter on Erosion

The rate of erosive wear is directly affected by the jet diameter. It is recommended to use multiple jets with smaller diameters to meet discharge flow requirements instead of depending on a single jet with a larger diameter [25]. The pressure head (H) exhibits a direct correlation with the jet diameter, while efficiency shows an inverse relationship. Specifically, the pressure head (H) is directly dependent on the jet diameter, while efficiency is inversely proportional to the jet diameter [26].

2.4 Techniques of Measuring Erosion

Diverse measurement methods are employed to calculate sediment erosion. The following section provides a comprehensive overview, encompassing the limitations associated with different measuring techniques.

2.4.1 Mass/Weight Loss Measurement

This method gauges the loss of eroded mass or weight using a physical balance with a specific least count. The accuracy increases with a higher least count and decreases vice versa. When dealing with a compact experimental setup, measuring thickness reduction becomes cumbersome due to least count limitations. Therefore, the recommended approach for estimating hydro-abrasive erosion is to employ the weight/mass loss technique [27].

In this technique, the specimen's mass is measured both before and after erosion, and the disparity between these values represents the mass loss caused by sediment erosion [25]. However, a limitation of this method is that it can only assess erosion for the entire specimen and not for specific regions of interest.

2.4.2 Thickness Reduction Measurement

A micrometer with 0.001 mm accuracy was used for measurements of thickness reduction. Reduction in thickness of material allows for the assessment of erosion in specific regions of the material. This technique provides insights into the material's behavior in different erosive environments and offers valuable information about erosion-induced changes in different areas of the material. It serves as a measurement parameter that complements weight loss measurements by providing a more localized view of erosion effects. The charm of thickness reduction is it can measure erosion in specific desired areas, which sets it apart from the mass loss technique [28].

2.4.3 3D Digitization

The favored approach for assessing erosion rates is this advanced technique, surpassing the other two methods, namely mass loss, and thickness reduction. In this methodology, a 3-D scanner is employed to intricately capture the surface profile of the specimen through the triangulation principle. Distinguishing itself from alternative techniques, this method not only delivers erosion rate data but also offers insights into erosion mechanisms, patterns, volume loss, and vulnerable areas to erosion. The overall accuracy of this approach falls within the range of 20 μm, and it

operates within a time limit of 2.5 seconds. Consequently, this technique boasts higher precision when compared to the other two methods.

2.5 Experimental and Numerical Investigation of Published Literature

Sr No	References	Material and erodent's	Methodology	Parameters varied	Results
1	Abdelaal et al. [29]	**Material:** Polylactic acid is made through FDM. **Erodent:** Silica with water (355µm-450 µm) 1 wt.%	Slurry erosion whirling arm rig	1-**Building orientation:** (vertical, horizontal and at 45º) **2-Layer thickness: (**0.1 mm,0.2 mm,0.3 mm) **3-Slurry impact angle** ($15^0, 45^0, 90^0$)	• The weight growth can be significantly affected by the impact angle and layer thickness. Water gain increases with thicker layers and decreases with higher impact angles. • Weight gain was not affected by building orientation and impact angles. • The number of particles that adhered to the sample surface was solely determined by the impact angle.
2	Correia et al. [30]	**Base Material:** Cylindrical-shaped mild steel. **Erodent:** silicon and oxygen with small traces of magnesium, aluminum, and calcium (125-250 µm)	Experimentation (SIJ setup)	**1-Slurry Velocities** (10, 13, 16, and 20 m/s) **2-Sand Loadings:** (300, 400, 500, and 600 mg/L) **3-Impingement angle**: 90^0	• As flow velocities and sand loadings rise, erosion levels intensify, leading to the creation of larger pits and noticeable ploughing tracks. • At lower flow velocities but with higher sand loadings, metal shards and cracks become more noticeable.
3	Singh Sidhu et al. [31]	**Material:** ABS and PLA **Erodent:** Silica (17,39,63,97 µm) with air	Ducom Air Erosive Testing Rig	**1- Impact Velocities:** (15,30,45,60 m/s) **2-Erodent size:** (17,39,63,97 µm) **3-Texture**	• The rectangular texture undergoes greater erosion compared to the prism texture. • As the size of the erodent, impact velocity, and time interval increased, the erosion rate also increased.

				(prism and square) **4- Impact angle:** **(**$30^0 - 90^0$) **5- time interval**	• It was discovered that PLA is harder than ABS, making it more resistant to erosion than ABS.
4	Chen et al. [32]	**Material:** Carbon steel **Erodent:** Silica (150 µm)	CFD-DEM	**1-Impact Angle:** (45º,60º,90º)	• It was documented that in single phase flow, the areas of maximum particle impaction are located adjacent to the exit for all three types of elbows. • The impact of the elbow angle on the erosion rate is significant, as it has a critical influence on particle motion.
5	Jukai Chen et al. [32]	**Material:** Carbon steel **Erodent:** Silica	HERTZ Minlin Contact Model (for particle-particle and particle wall contact)	**Particle diameter:** 150um **Density:** 2650 kg/m^3 **Inlet velocity:** 3 m/s	• This study presents an erosion prediction model for liquid-particle flow in pipeline elbows. The model considers various interactions and uses computational simulations to forecast the maximum erosion rates and locations in elbows of different angles. • The findings indicate that the maximum erosion rate occurs near the exit of the elbows, with higher rates in larger bend angles. The projected erosion locations are consistent with both simulation and experimental observations. • In a 90° elbow, a greater number of particles impact the wall at lower velocities, while higher particle incidence angles are observed due to increased rebounds and inter-particle collisions.
6	Peng w et al. [33]	**Material:** Carbon steel	CFD **Erosion models:** (Ahlert	**Diameter:** 50 to 300um **Density:**	• The study utilizes a two-way coupled Eulerian-Lagrangian approach to predict erosion in

			erosion model, DNV erosion model, E/CRC erosion model, Neilson and Gilchrist erosion model, Oka et al erosion model)	2650 kg/m^3 **Mass flow rate**: 0.2 kg/s Velocity: 5 to 25 m/s	pipe bends. The E/CRC erosive wear model yields the most accurate results when compared to experimental data. • The analysis highlights the significant influence of parameters such as pipe diameter, inlet velocity, bending angle, particle mass flow, particle diameter, and bend orientation on erosion behavior.
7	Xiao et al. [34]	**Base Material:** Carbon Steel elbow shaped. **Erodent:** SiO2	CFD and DEM	**1-gas velocity** **2-moisture content** **3-impact velocity** **4-impact angle**	• Particle-particle collision increases at the curvature, leading to a reduction in impact velocity, which in turn affects the rate of erosion. • An increase in moisture content leads to a higher erosion rate, with wet particles being more responsible for erosion than dry particles.
8	Lei Xu et al. [35]	**Material:** Aluminum	**Mathematical model and numerical method:** **Erosion model:** a particle-scale erosion model, SIEM **Simulation conditions:** The SIMPLEC method was adopted in FLUENT software to solve the governing	**Density (kg/m3):** 2650 **Diameter of the particle (**μm**):** 150 **Mass flow (kg/s):** 0.000208, 0.00208, 0.0208, 0.208 Inlet **velocity of air (m/s):** 45.72	• A new erosion model, the Shear Impact Energy Model (SIEM), is utilized to investigate elbow erosion through numerical simulations using the CFD-DEM coupling method. • The study investigates the effects of particle movements, forces from the fluid, and micro-scale models (CFD-DPM and CFD-DEM) to accurately predict erosion in elbows. • The study analyzes the wear rate distribution along the extrados of the elbow, revealing a decrease in wear

			equations for airflow.		from 50-70° and minimal wear beyond 70° due to variations in shear impact energy.
9	Vieira et al. [36]	**Material:** Stainless Steel **Erodent:** Silica	Flow Loop Non-Intrusive Ultrasonic Technique (UT)	**Particle size:** 150 µm and 300µm	• It was noted that in the case of single-phase flow with sand, the point of greatest erosion was determined to be at 45º. • The particle size was observed to have no significant effect on erosion rate in single-phase flows. However, it was found that the 300 µm sand degrades material between 1.9 to 2.5 times more compared to the 150 µm sand.
10	Chen et al. [32]	**Material:** Carbon steel **Erodent:** silica	CFD-DEM	**Particle size:** 150 µm **Impact angle:** (45º,60º,90º)	• The report indicated that in single-phase flow, the maximum particle impaction locations are adjacent to the exit for all three types of elbows. • The impact of the elbow angle on the erosion rate is significant due to its critical influence on particle motion.

2.6 Flow patterns of slurry in a horizontal pipe

2.6.1 Effect of viscosity

The velocity of erodent particles is altered by the characteristic of the carrier fluid, such as viscosity, and therefore plays an important role in controlling erosion. The slurry, which carries the erodent particles, acts as both a coolant and a lubricant, helping to minimize erosion by reducing the direct impact of particles on the material. Tang et al. [22] conducted a study on the effect of fluid viscosity on erosive wear using Ti (C, N)-based cermet's and five different fluids with varying viscosities. Among these fluids, those with a 5% concentration of $Al_2 O_3$ became more viscous and were able to restrict the impact of erodent particles by reducing flow velocity. This decrease in erodent impact energy can be attributed to increased adhesion between layers of

slurry, causing the velocity of erodent particles to decrease.

2.6.2 Effect of multiphase flow

Multiphase flow involves the movement of multiple phases of matter, such as solid, liquid, and gas, through a pipe or specific environment. It is utilized in various applications, including petroleum and chemical transportation. While understanding the flow condition in a single phase is relatively straightforward, in multiphase flow, the phases do not have a uniform distribution. This can lead to significant impact on flow patterns due to interactions between the phases.

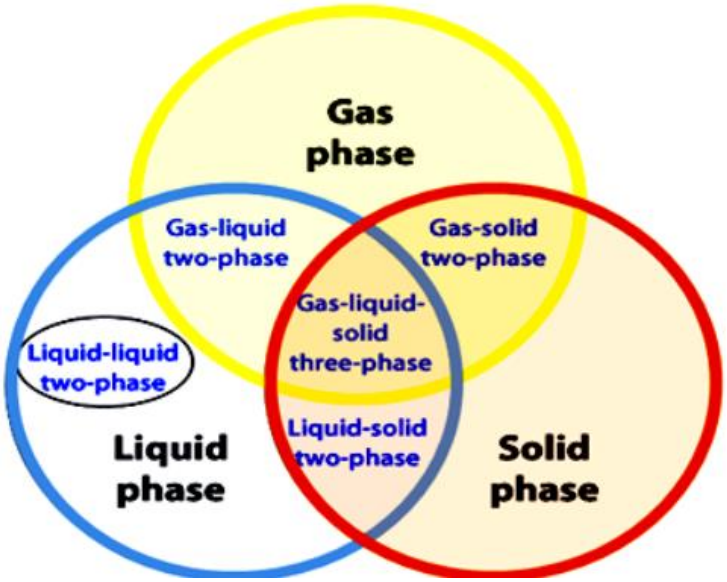

Figure 2.7: Solid-liquid and gas flow segregation.

2.7 Flow patterns of slurry in horizontal pipes

Flow patterns of slurry in a pipe are predominantly determined by the flow velocities [23]. The accompanying Figure 2.8 illustrates the various flow patterns that can occur in a horizontal pipe when considering the distribution of solid, liquid, and gas phases. It is essential for engineers involved in system and model design to thoroughly investigate the different types of flows characterized by the movement of different phases within the conduit or pipe. By studying these flow patterns, engineers can effectively optimize the design and performance of systems handling slurry flow.

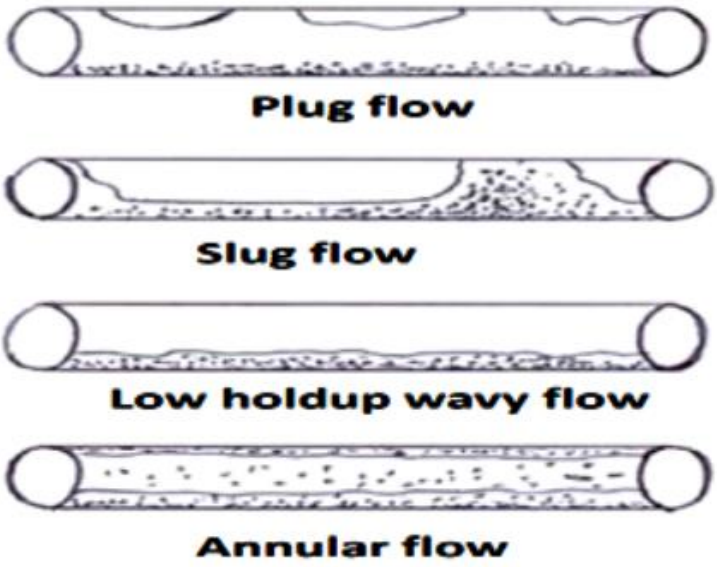

Figure 2.8: Flow distribution in pipes [24]

2.7.1 Plug Flow

Plug flow is the unique and separate movement of two different phases within a conduit, like a pipe or channel, where their distinct densities keep them apart. In this flow pattern, the phases are characterized by the uniform movement of plugs, representing distinct portions of each phase, near the intact cross-sectional area of the pipe. This flow pattern enables the preservation of phase separation and is frequently seen in multiphase flow systems. Understanding plug flow is crucial in numerous industries, especially those involved in the transportation and processing of multiphase fluids.

2.7.2 Slug flow

Slug flow occurs due to the interaction between gas and liquid phases, resulting in periodic movements of these phases. In this flow pattern, the liquid phase forms separate slugs that are interspersed by the gas phase, creating a pattern of alternating liquid slugs and gas bubbles. Slug flow is often encountered when both phases flow at intermediate velocities and is commonly observed in industries involved in the transportation of oil and gas. Understanding and managing slug flow behavior is essential for efficient operation and system design in these industries.

2.7.3 Low Hold up wavy flow

Low hold-up wavy flow is defined by a wavy distribution of the liquid phase along the inner side of the pipeline, with waves taking the form of ripples and containing a relatively small volume of liquid. In the context of liquid hold-up wavy flow, "hold-up" refers to the region occupied by the liquid phase. This flow pattern is seen as a transitional state between slug flow and annular flow, representing an intermediate phase between these two patterns.

2.7.4 Annular flow

Annular flow is defined by the simultaneous existence of both liquid and gas phases. In this flow pattern, a continuous film of liquid adheres to the inner walls of the pipelines, while the central region is filled with the gas phase, which does not meet the conduit's walls. This configuration creates an annular pattern, reflecting the name given to this flow pattern. Compared to other multiphase flows, annular flow shows lower turbulence. Furthermore, annular flow is more likely to occur when the velocity of the gas phase exceeds that of the liquid phase.

2.8 Flow patterns segregation in two phase flow

The segregation of gas and liquid phases within a flow system is represented by transitional zones, providing valuable insights into the underlying flow patterns captured in two-dimensional flow pattern maps [25], [26]. These flow patterns are empirically determined, utilizing industrial observations while considering influential factors such as pipe diameter and the angle of fluid impact. The properties of both phases, including density and viscosity, are also carefully considered in the development of these flow patterns.

Figure presented showcases the flow maps employed by Mandhane [25] and Baker [26] respectively. These maps utilize superficial gas and liquid velocities as key parameters for mapping flow patterns and identifying segregation zones within the system. By employing these maps, a comprehensive understanding of the flow behavior and phase distribution can be achieved.

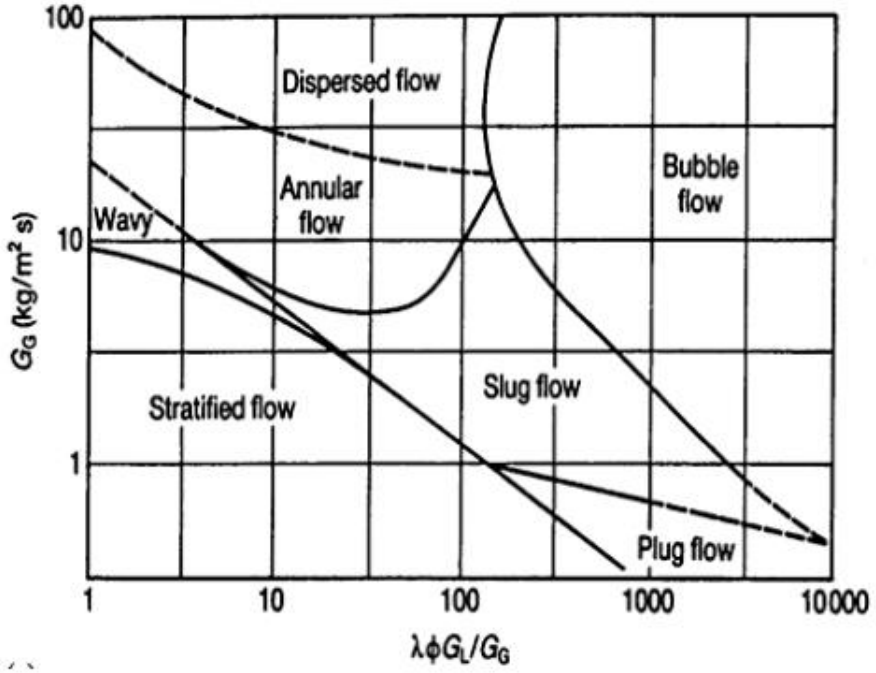

Figure 2.9: Baker flow-map for two phase conduit flow [24]

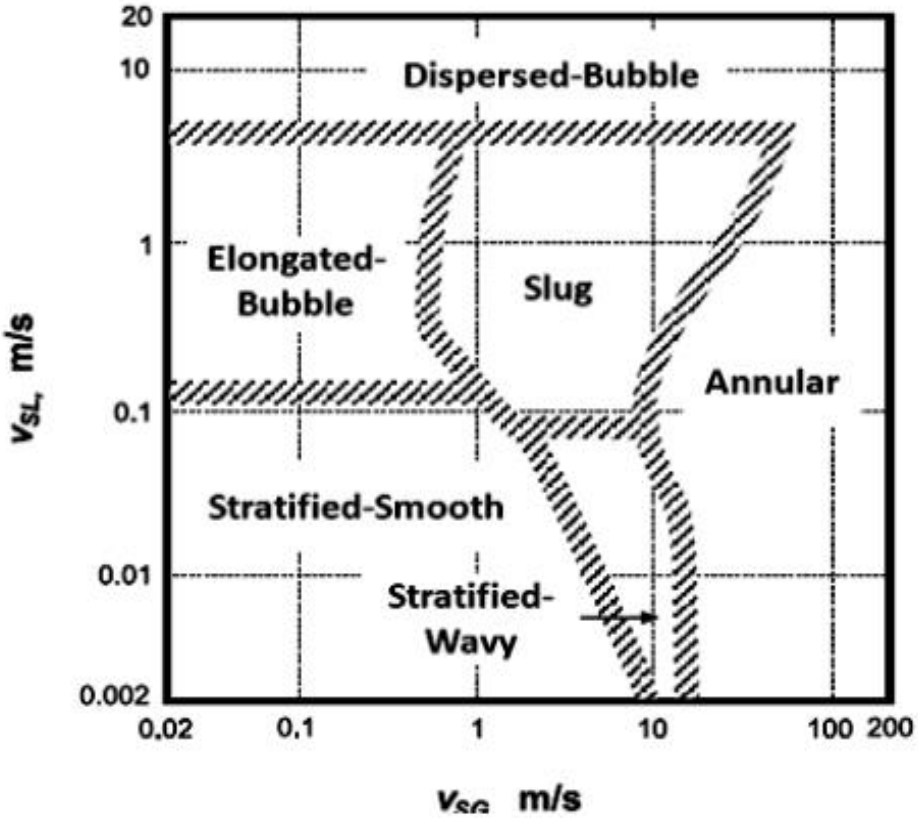

Figure 2.10: Mandhane flow-map for two phase conduit flow [23]

2.9 Types of Erosion Tests

Researchers have developed various types of test rigs to assess erosive wear under diverse operating conditions. While these test rigs may differ in characteristics and working conditions, the fundamental erosion mechanism remains consistent. A comprehensive examination of different test rigs is provided below.

2.9.1 Pot Erosive Wear Test

The pot erosive wear test is employed to assess the erosion resistance limits of materials. This experimental arrangement is straightforward to operate for evaluating erosion resistance. In this setup, the test sample, placed on a spindle, rotates, and is immersed in a slurry pot. The high-speed rotation of the sample against the slurry results in impacts on the surface, causing the removal of the impingement zone because of particle striking. The erosive wear rate is determined by calculating weight loss. However, a notable drawback of this test lies in the turbulence induced within the pot, which poses challenges in obtaining meaningful measurements. The schematic of the setup is depicted in Figure 2.11, featuring a pot with a central rotating shaft connected to mount the test samples. Baffles are strategically placed on the inner wall of the pot to ensure effective blending of the slurry.

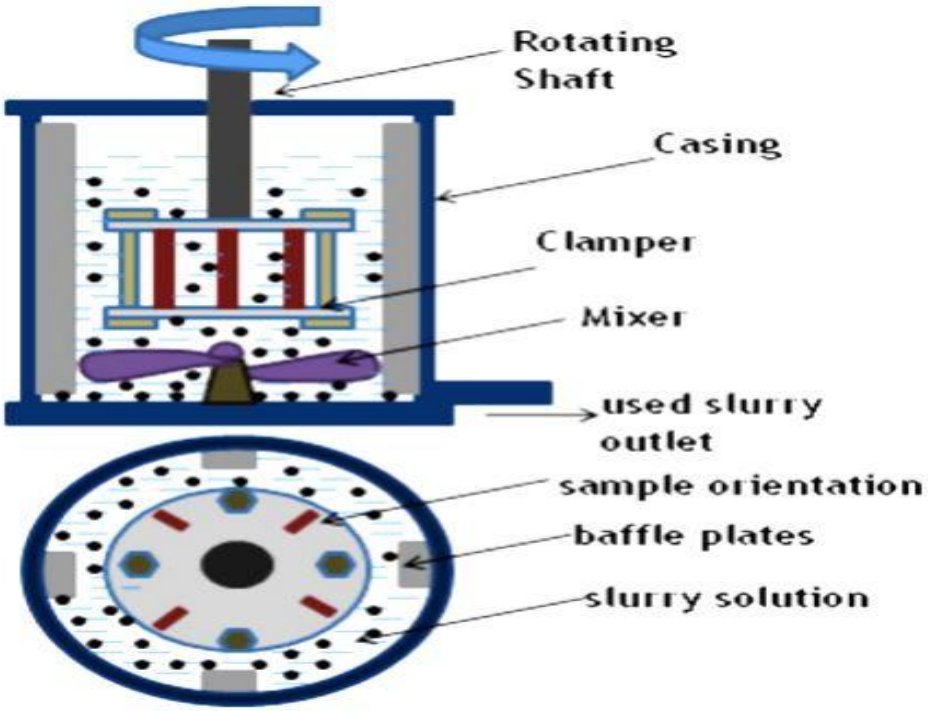

Figure 2.11: Schematic presentation of pot-type slurry erosion test rig [37]

2.9.2 Direct Impact Test

This test is also known as the impingement jet test and is frequently employed by researchers in the field. The setup includes an air compressor, sand feeder, and a nozzle. The air compressor is utilized to achieve the desired speed at the nozzle outlet, while sand particles are fed through the feeding tube. The blend of air and sand particles escapes through the nozzle outlet at the desired speed and impacts the target surface at multiple angles. This method is favored for its flexibility in controlling flow speed and impact angle. The schematic of this setup is depicted in figure 2.12.

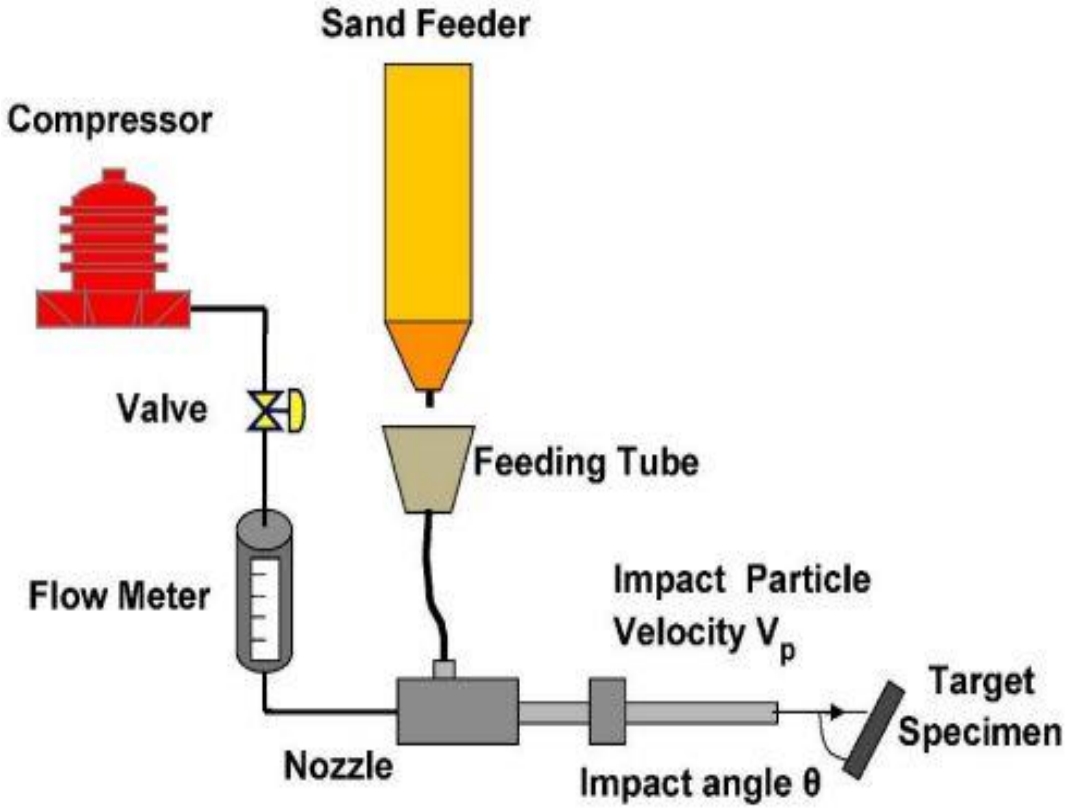

Figure 2.12: Direct impact testing rig schematic diagram[36]

2.9.3 Coriolis Test

The Coriolis erosion tester includes a steel rotor with a channel, where two circular section specimen holders are placed with approximately 0.05 mm clearance on the opposite side of the rotor. Each specimen holder has a channel with a flat plate forming the base. The slurry is delivered to the central chamber and is flung outgoing as the rotor begins to rotate. The Coriolis acceleration causes the slurry particles to settle out and impact the target surface of the specimen. The schematic of this method is depicted in figure 2.13.

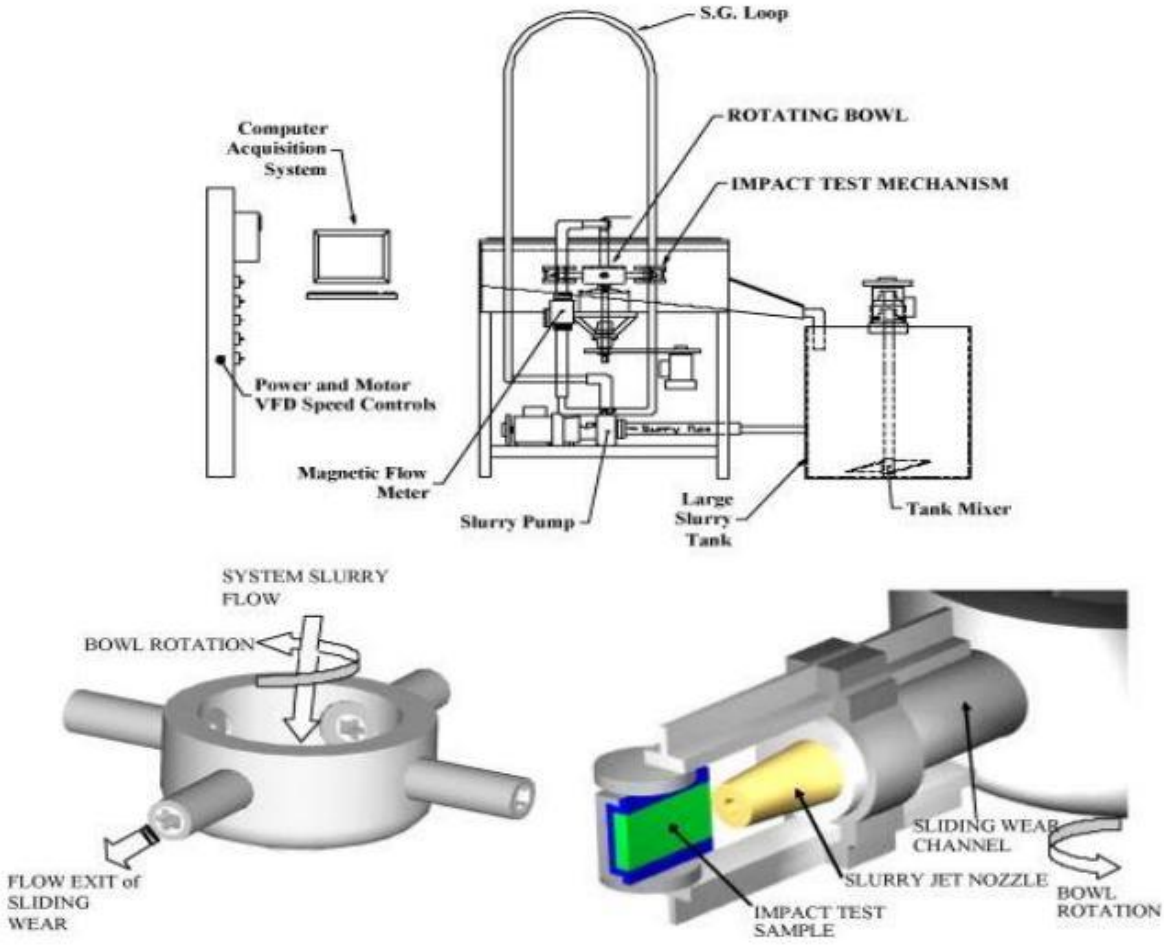

Figure 2.13: Schematic of Coriolis Erosion Test [38]

2.9.4 Flow loop testing rig

Numerous researchers have employed a flow loop test bench with the ability to adjust the flow for studying erosive wear. Figure 2.14 depicts a schematic representation of the flow loop test bench utilized by Parsi et al. [32]. This bench involves the interaction of solid, liquid, and gas phases, aiming to replicate real-world scenarios. It offers valuable insights into erosion rates occurring in single-phase and as well as in multiphase flow. However, it lacks the capability to control erodent impact conditions and impingement angles. As a result, it is not deemed suitable for studying erosion models that require detailed information about erodent dynamics.

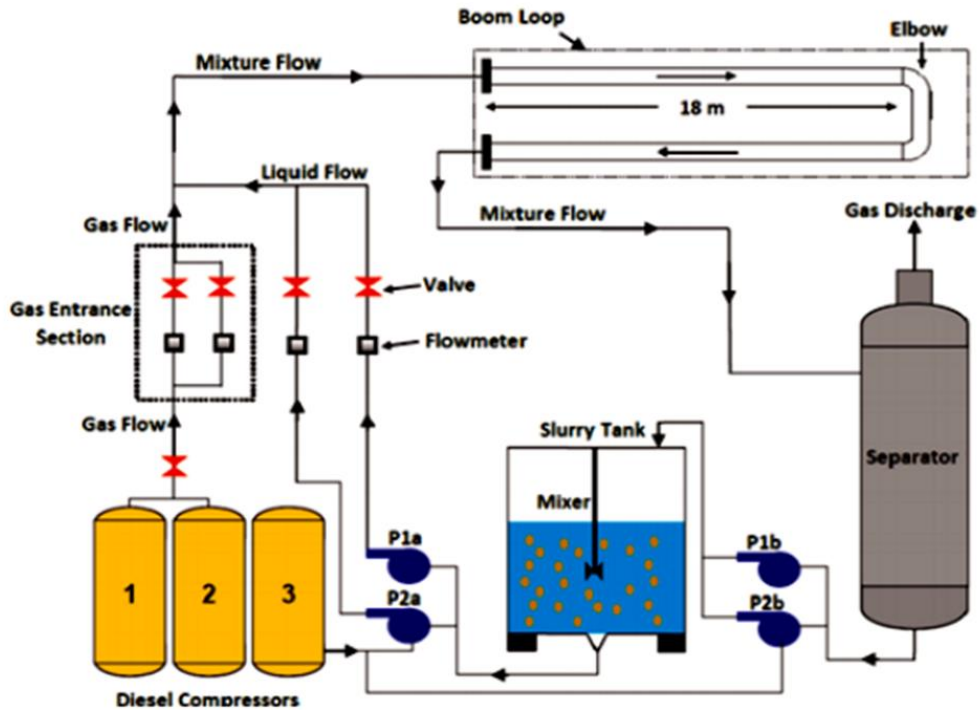

Figure 2.14: Multiphase flow erosion test loop schematic diagram [39]

2.10 Summary

This chapter presents a thorough examination of the existing literature on erosion, with the goal of offering a comprehensive insight into the subject. The review explores various factors contributing to erosion, such as particle angle, velocity, size, temperature, particle concentration, and the influence of long radius elbows. These factors are discussed in detail, emphasizing their respective roles in causing erosion.

Furthermore, the chapter delves into three different methods for calculating erosion rate. The first method involves measuring thickness reduction to directly indicate erosion, the second method uses weight loss measurements to assess mass loss caused by erosion, and the third method, 3-D digitalization, is introduced as a modern technique for quantifying erosion and providing a comprehensive analysis. Each method is thoroughly examined, highlighting their advantages and limitations in accurately assessing erosion.

The chapter also underscores the significance of different flow conditions and their relevance to erosion. It discusses the impact of various flow patterns and their implications for erosion mechanisms, as well as the importance of multiphase flow in relation to erosion phenomena.

Finally, the literature review summarizes the findings of previous researchers in the field, providing an overview of their studies and highlighting key discoveries and contributions to the understanding of erosion. By synthesizing this existing body of research, a comprehensive understanding of the subject matter is achieved, enabling further advancements in the field of elbow erosion prevention and mitigation.

CHAPTER 3 : METHODOLOGY

3.1 Introduction

This chapter presents a comprehensive summary of the research methodology employed in this study. Section 3.2 provides detailed information on the materials used, experimental setup, testing conditions, and sample preparation. The chapter also explains the various measurement methods used to calculate erosion, and the significance of input parameters was determined using techniques such as Taguchi ANOVA.

A variety of qualitative and quantitative methods were used to evaluate the rate of degradation and thickness loss in different sections of the eroded surface in a multi-phase flow. Additionally, the mass of the samples was measured before and post experimentation, helping to identify erosion and degradation under various conditions. Two distinct sets of experiments were conducted, using Sand-Liquid flow and SAND-Liquid-Air as multi phases, respectively, and following the Taguchi array. Scanning Electron Microscopy (SEM) was used to give a thorough understanding of the rate of erosion and degradation. Furthermore, the values of the erosion rate were explained using response surface methodology (RSM).

3.2 Specimen Details

The creation of samples involved utilizing Poly-Lactic Acid (PLA), a biodegradable thermoplastic produced from the fermentation of sugarcane or corn starch. This fermentation process converts starch into sugars, particularly glucose, which then leads to the generation of lactic acid. Lactide, a cyclic ester, is subsequently formed through the esterification of this lactic acid. These lactide monomers go through polymerization to build long chains of PLA, using methods such as ring-opening polymerization. The methods for producing Poly-Lactic Acid are shown in Figure 3.1.

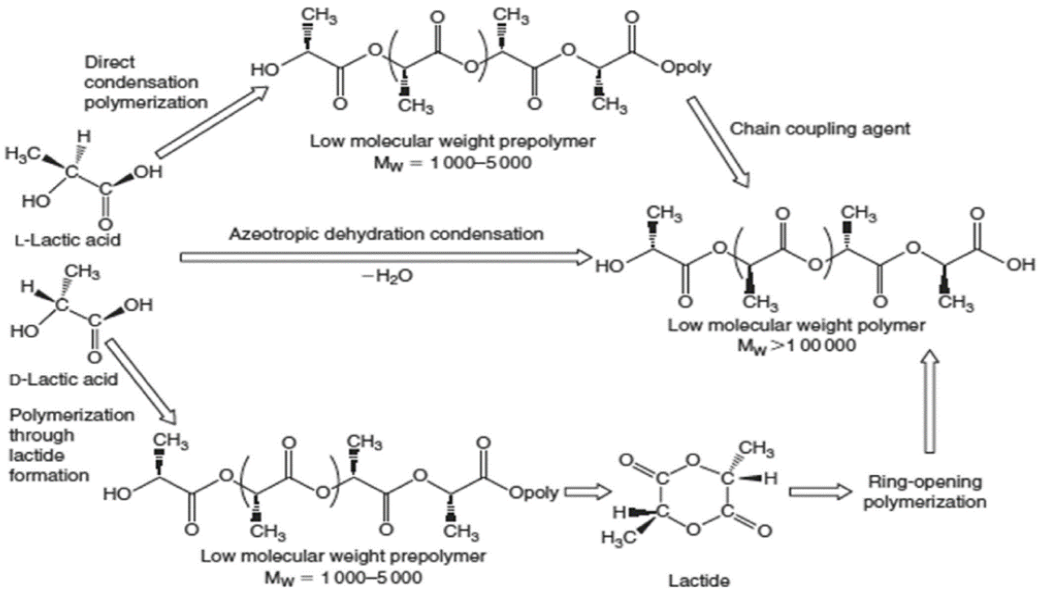

Figure 3.1: Schematic diagram of preparation of PLA [40]

The decision to use PLA as a material for sample preparation is based on its high strength, stability, sustainability, biodegradability, transparency, and versatility, making it suitable for many applications like medical science and packaging. PLA can be molded into filaments that can be used for 3D printing of complex shapes and geometries. The specifications of PLA filament used for 3D printing of flat plate samples are shown in Table 3.1.

Table 3.1: Filament specifications

Filament Specifications		
Size	**Tolerance**	**Length**
1.75 mm	0.03 mm	335 m
Material properties		
Density	ISO 1183	1.24g/cm
Melt flow rate (210 °C)	ISO 1133	8.1 g/10min
Melt Temperature	DSC	168°C
Recommended Printer Setup		
Extrusion Temperature	210 ± 10°C	
Printing speed	30 mm/s	

3.3 Specimen Preparation

The specimens were created using a Fused Deposition Modeling (FDM) 3D printer. The sample preparation process begins with designing a 3D model using Computer-Aided Design (CAD) software, such as SolidWorks in our case. This digital model is then sliced using Ultimaker Cura version 5.4.0, a process that involves dividing the model into horizontal layers and generating instructions (G-codes) for the 3D printer. FDM technology uses PLA filament, which is heated in the printer's extruder. As it reaches a molten state, it is deposited layer by layer onto the printer's bed. This layer-by-layer 3D printing technique allows for the precise formation of the desired geometry along the X, Y, and Z axes. A visual representation of a typical 3D printing process is shown in Figure 3.2.

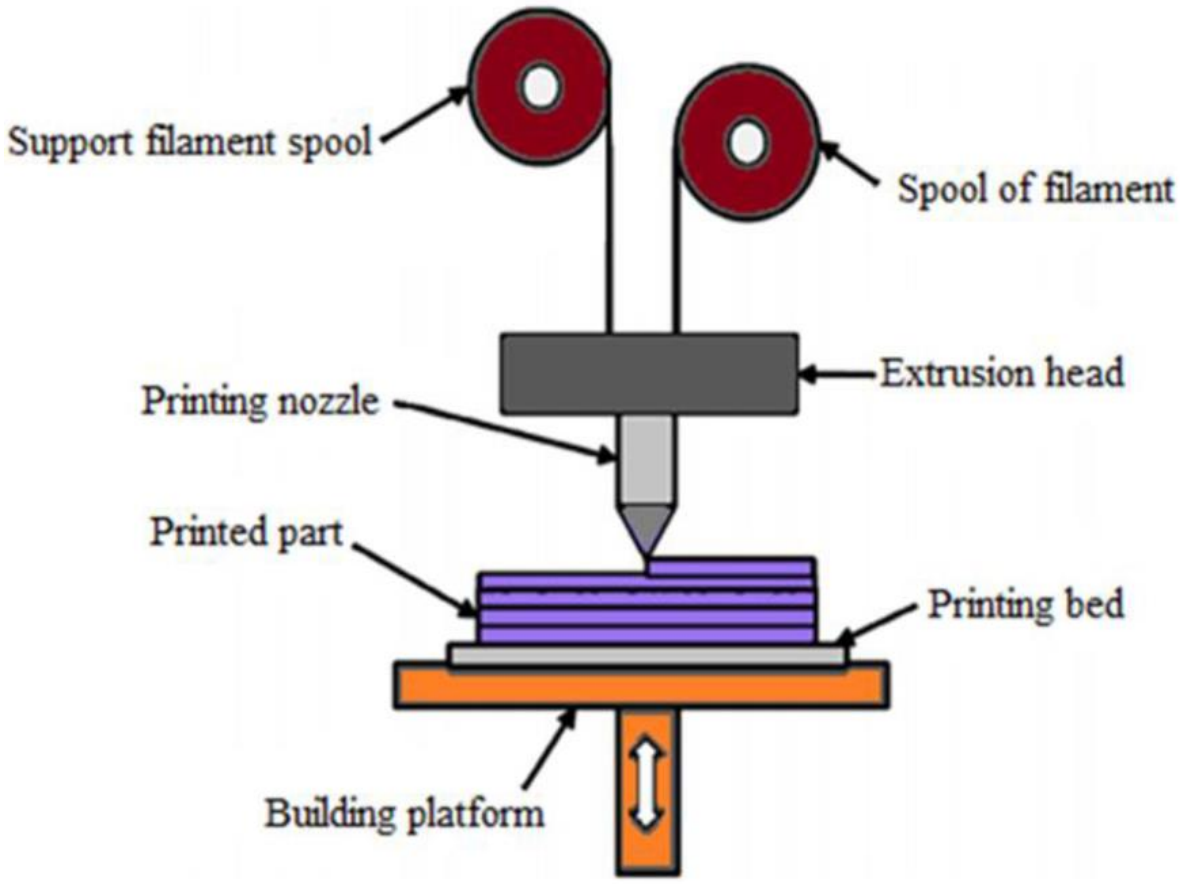

Figure 3.2: Schematic diagram of the Fused Deposition Modelling Process [41]

After setting up the printer in Ultimaker Cura 5.4.0, 3D printing was performed using the Ender-3 Pro integrated 3D printer. All printed samples maintained an infill density of 20%. The geometrical

specifications of the test samples are outlined in Figure 3.3. Printing conditions included a temperature of 210 °C, a printing speed of 30 mm/s, and a heated bed surface maintained at 60 °C.

Additionally, PLA samples with subsurface textured surfaces, featuring zigzag, concentric, and grid patterns, were 3D printed with an infill density of 20%, as shown in Figure 3.3. While various subsurface textured surfaces have been used in previous research, the usage of zigzag, concentric, and grid patterns has been limited, despite their ease of printability. These samples, measuring 38 mm x 38 mm with a thickness of 3.82 mm, showcasing the initial weight and thickness of the samples. Although the initial thickness remains consistent across all 3D printed samples, there is a variation in sample weight attributed to the geometric arrangement of the infill pattern, which dictates the material consumption during preparation. The concentric texture, featuring more spaces, contrasts with the continuous lines of zigzag and grid patterns, influencing overall material consumption. These parameters play a crucial role in determining the overall strength, rigidity, and printing time during sample preparation, as summarized in Table 3.1.

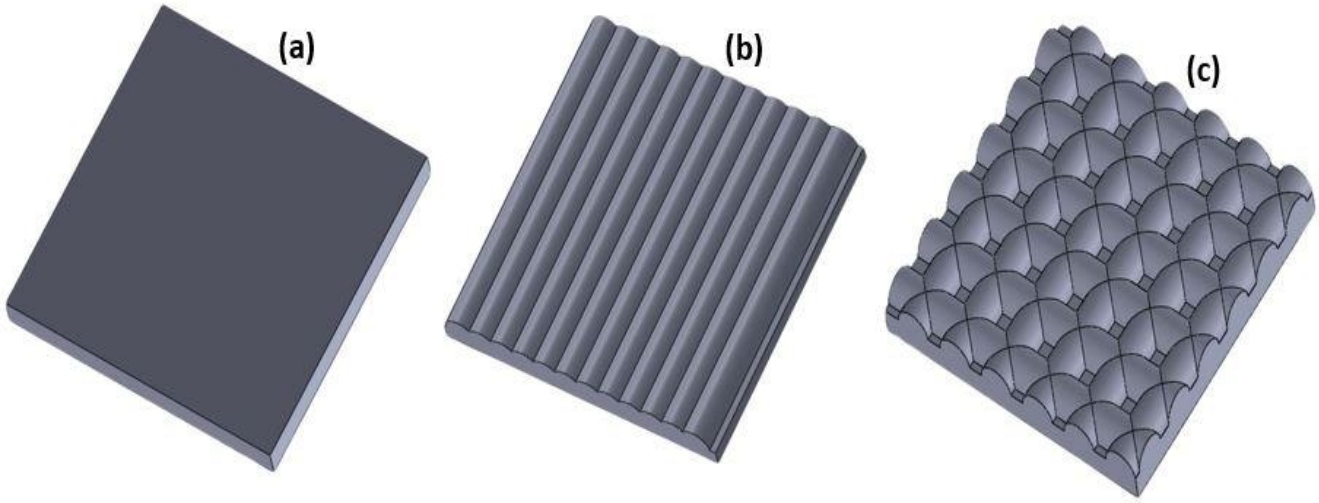

Figure 3.3: Designs (a) D1 (Flat) (b) D2 (Groove) (c) D3 (Square groove)

3.4 Experimental Apparatus

The experiments were conducted using the experimental test bench depicted in Figure 3.4. The setup included a slurry with a specific pH value, a flowmeter, a sewage submersible pump, a tank, a sample holder, a stirrer, and a glass casing. Furthermore, different sets of erodent's were used to conduct experiments following the L9 Taguchi array. Components description of the various components used for the experiments is presented in the following sections.

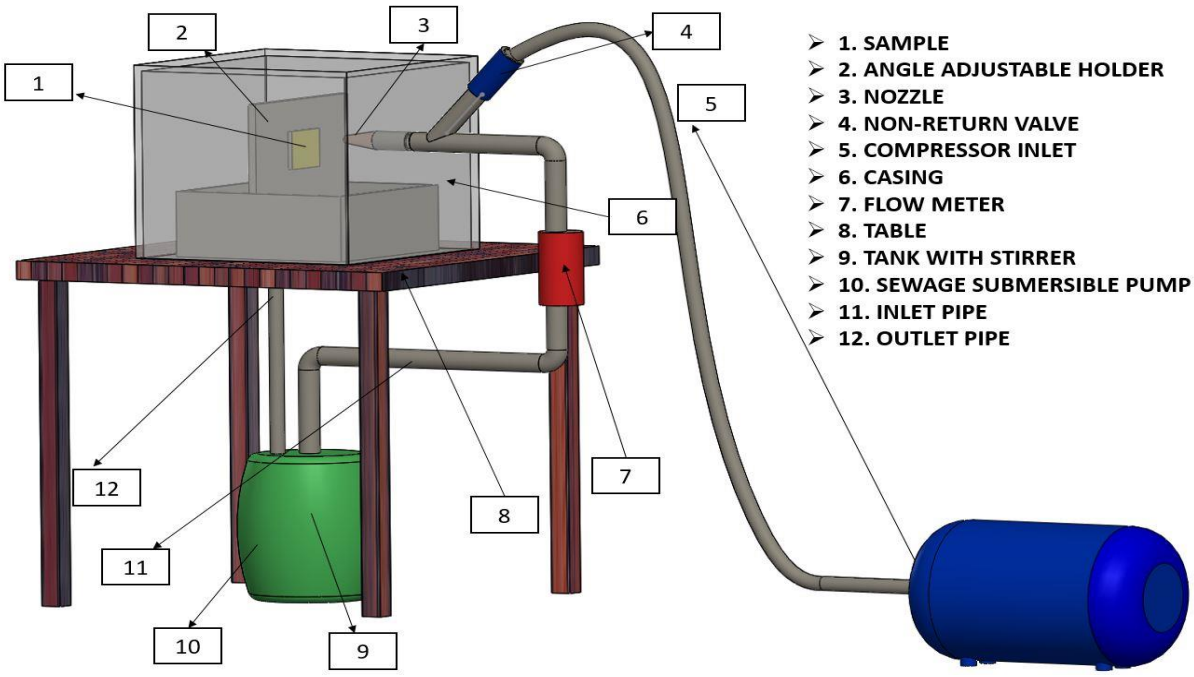

Figure 3.4: Slurry flow testing rig experimental apparatus

3.4.1 Sample holder

A precisely dimensioned sample holder, measuring 184 mm x 92 mm, was carefully manufactured using CNC machining. It features a square-shaped cavity measuring 38 mm x 38 mm and was made from aluminum. To secure the samples during testing, a combination of bolts and nuts was used for clamping within the holder, allowing for angle adjustments to facilitate testing at various orientations. The visual representation of the utilized sample holder is shown in the accompanying Figure 3.5.

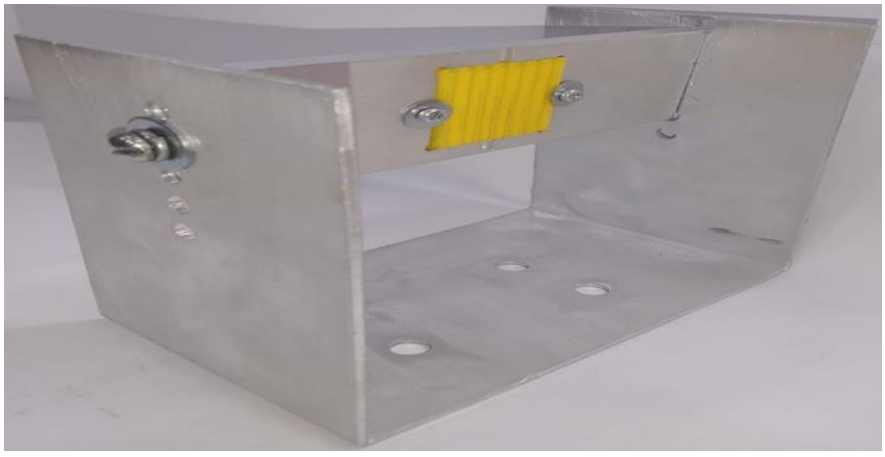

Figure 3.5: Sample holder for clamping sample

3.4.2 Erodent's

Erosion is affected by attributes of the erodent, such as its size, shape, and hardness [42]. Natural silica sand within the nominal size of 300 µm was employed as the erodent, combined with tap water to create a solid–liquid slurry. Figure 3.6 shows the microscopic illustration of the erodent. Observing the image reveals a distinctive pattern where the particles demonstrate a relatively uniform and block-like structure.

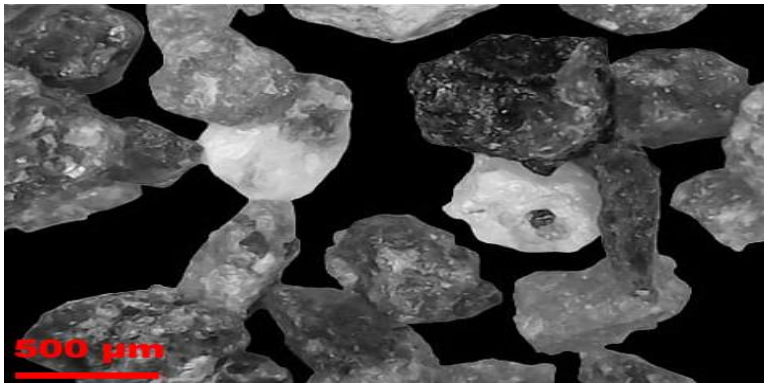

Figure 3.6: Microscopic image of natural silica sand

3.4.3 Flowmeter

During the experimentation, it was essential to determine the fluid flow rate. The velocity of the fluid was measured using a turbine flowmeter, as shown in figure 3.7, which is specifically designed to measure fluid flow by utilizing the rotation of its turbine. To evaluate the speed of the fluid, a rotating turbine is placed in the liquid flow, and the speed of its rotation provides important parameters such as velocity and fluid flow rate. Turbine flowmeters are widely used in industries including oil, gas, and chemical sectors due to their effectiveness in accurately measuring fluid flow.

Figure 3.7: Turbine flowmeter utilized for experiments.

3.5 Measurement method

3.5.1 Thickness loss Method

Using this approach enables the detection of erosion in specific areas of the target material, providing researchers with a way to understand the material removal caused by erosion in different regions. This investigation provides valuable insights into how the material behaves in various erosive environments [43]. The method allows for a comprehensive understanding of different material sections' responses to erosion, thereby significantly contributing to the advancement of materials with high erosion resistance. Determining variations in thickness in various eroded regions is particularly important in applications where erosive wear is a critical factor. This research approach sets the groundwork for improving materials to effectively withstand erosive challenges.

3.5.2 Scanning Electron Microscopy

Scanning Electron Microscopy (SEM) is an advanced approach utilized for examining the structure and properties of samples at atomic and molecular levels. It is commonly employed to study surface morphology, topography, chemical composition, and crystalline structure at high resolutions. SEM employs a focused beam of high-energy electrons to produce high-resolution images of the sample's surface. The operational principle of SEM is briefly described below:

1. The specimen is prepared to fit the dimensional constraints of the Scanning Electron Microscope (SEM).
2. The prepared specimen is placed in a vacuum, and a beam of high-energy electrons is generated using an electron gun.
3. Electromagnetic lenses are used to focus the beam of high-energy electrons on the desired surface of the specimen.
4. When the beam of high-energy electrons strikes the target surface, it interacts with the surface atoms, emitting secondary electrons.
5. A detector is employed to capture the emission of secondary electrons, generating a signal used to produce high-resolution images of the target surface. In this research, SEM was used to capture high-resolution images of the impact surface of the specimens. The specimens were cut into small specimens measuring 7 × 7 mm using a hacksaw blade

machine. The high-resolution SEM images were then analyzed to investigate the erosive wear pattern and mechanism in different samples. Indentation, ploughing, pits, and cutting erosion mechanisms on the specimen's impact surface were observed using SEM images. Additionally, SEM images were utilized to identify the chemical composition of the specimen's materials.

3.5.3 3D Scanning

3D scanning is an advanced technology used to capture the three-dimensional geometry of an object or physical environment. The working principle of 3D scanning is briefly outlined below.

1. The initial step of 3D scanning involves capturing the physical object or specimen using laser light. The 3D scanner emits structured light signals to measure the reflection/distortion and capture the shape and texture of the target object.

2. The raw data collected from the 3D scanner in the form of signals is then processed to generate a 3D model of the target object. Processing the raw data involves removing noise and other errors and converting it into a usable format.

3. The final step involves refinement, checking for any inappropriate capturing or imperfections. In this research, 3D scanning was used to obtain the physical structure and precise dimensions of the specimens using laser technology. 3D models of all eighteen specimens were obtained before and after the erosion test using a hand-held 3D scanner. The 3D scanned models have various applications, including precise measurement, 3D modeling, inspection and analysis, manufacturing and prototyping, customized manufacturing, medical and cultural heritage preservation. In this research, the 3D models of each specimen were used for inspection and analysis of wear and tear on the impacted surface. A schematic of 3D scanning is presented in Figure 3.8, and a detailed discussion of the 3D scanning results is given in the results section.

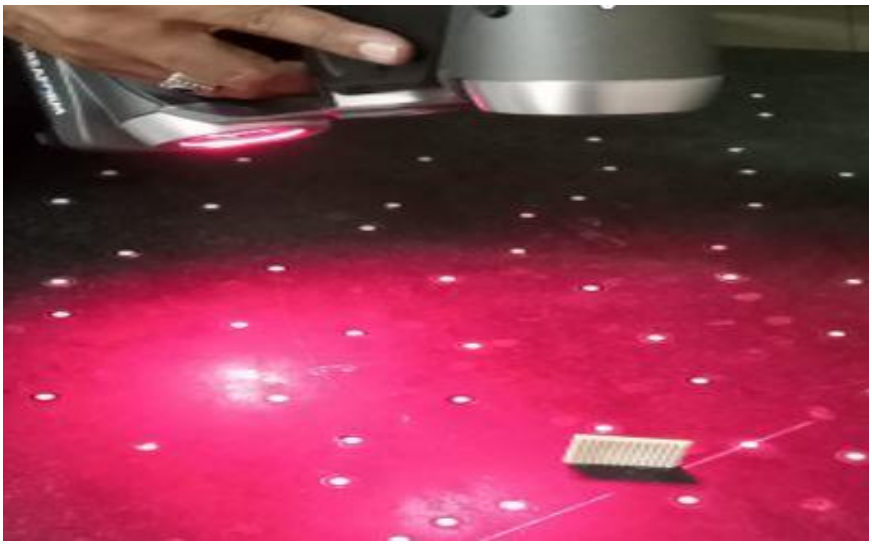

Figure 3.8: Scanning samples using Hand-Held 3D scanner.

3.6 Design of Experiments

In this experimental investigation, the erosive wear of PLA was quantified by manipulating various influencing parameters, including design, concentration, and impact angle as depicted in Table 3.2. Previous research has demonstrated the influence of these characteristics on erosion wear [44], [45]. This study employed a Taguchi L9 design, as illustrated in Table 3.3, considering three levels for the experiments.

Table 3.2: Input parameters Taguchi Array of Experiment for water experiments

Input Parameters			
Parameters	Level 1	Level 2	Level 3
Design	1	2	3
Concentration wt.%	5	3	1
Angle^{o}	90	75	60

Table 3.3: Taguchi L9 Array for water

Run #	Design	Concentration wt.%	Angle^{o}
1	D1	1	60
2	D1	3	75
3	D1	5	90
4	D2	1	75
5	D2	3	90
6	D2	5	60
7	D3	1	90
8	D3	3	60
9	D3	5	75

3.7 Orthogonal Arrays

The design of experiment was employed to optimize the erosion wear of PLA material. Typically, erosion wear parameters cannot be optimized directly, as the issue is intricately linked to the increase or decrease of specific parameters. Minimizing the values of influencing parameters tends to result in the minimum erosion wear. In alignment with the objective of this study, the crucial task was to identify the most influential parameter among various factors. To achieve this, Taguchi's method was employed [46], [47].

3.8 Taguchi Method

The modeling and analysis of the impact of control factors on performance output are conducted using Taguchi's parameter design approach. The selection of control factors is a critical aspect of the design of the experiment. The conditions in which erosion tests are performed are provided in Table 3. The tests are carried out following the experimental design shown in Table 3 at room temperature. In this study, three parameters design, concentration and impingement angle are considered, each at three levels, following an L9 orthogonal design. In Table 3, each column

represents a test parameter, and a row gives a test condition, representing a combination of parameter levels.

The experimental data are converted into a signal-to-noise (S/N) ratio, with various S/N ratios available depending on the type of characteristics. The S/N ratio characteristics can be categorized into three types as given by Equations. (1)-(3) [48] when the characteristic is continuous:

3.8.1 Larger the Better

When the "larger is better" criterion is applied, the objective is to identify various combinations of factors that result in the maximum output parameter. This approach considers the highest value of the output parameter as optimal. The "larger the better" calculation is typically performed as follows [49].

$$\frac{S}{N} = -10\log\frac{1}{n}\left(\sum\frac{1}{Y^2}\right) \quad (1)$$

3.8.2 Nominal the best:

Nominal the best is applied when the goal is to achieve a target level of value and thus uses a combination of different factors which leads to the nominal output parameter value. Nominal the best [50], [51] is calculated as follows:

$$\frac{S}{N} = -10\log\frac{1}{n}\left(\sum\frac{\bar{Y}}{S_Y^2}\right) \quad (2)$$

3.8.3 Smaller is better:

The "smaller the better" criterion is employed when the objective is to minimize output parameters. This methodology involves identifying combinations of different factors that lead to the minimum output parameter. In the "smaller the better" approach, the calculation is typically performed as follows [52]

$$\frac{S}{N} = -110\log\frac{1}{n}(\sum Y^2) \quad (3)$$

where $\bar{Y}$ is the average of observed data, S_Y^2 the variation of y, n the number of observations, and y the observed data. “Lower is better” (LB) characteristic with the above S/N ratio transformation is suitable for minimization of erosion rate.

3.8.4 Delta Values:

Delta values represent the variance between the maximum and minimum S/N (signal-to-noise) values for individual parameters, which are then ranked. The parameter with the greater S/N value is considered predominant, and the ranking is based on this parameter.

3.9 Analysis of Variance (ANOVA)

The objective of the (ANOVA) is to inquire into the significant effect of design parameters on the quality characteristic. This is achieved through breaking down the overall variability of the signal-to-noise (S/N) ratios, calculated as the summation of squared deviations from the overall mean of S/N ratio, and attributing these variations to individual design parameters as well as errors. Initially, the overall summation of squared deviations (SS_T) from the overall average of S/N ratio $\bar{y}$ is computed using equation (4) [53], [54].

$$SS_T = \sum_{i=1}^{n} (y_i - \bar{y})^2 \qquad (4)$$

Here, *n* represents the No of experiments in the orthogonal L9 array, and y_i is the average signal-to-noise (S/N) ratio for the ith experiment.

$$\bar{Y} = \frac{1}{N}\sum_{i=1}^{N} Y_i \qquad (5)$$

Sum of squared deviations SS_T contains sum of squared error SS_e and sum of squared deviations SS_P due to every process parameter. Therefore, it is defined as by equation 6 [55].

$$SS_P = \sum_{j=1}^{t} \frac{(SY_j)^2}{t} - \frac{1}{N}\left[\sum_{i=1}^{N} Y_i\right]^2 \qquad (6)$$

Here

P= one of the parameters

j= level of parameter P

t= iterations of parameter P

SY_j= Sum of experimental results compromising of parameter P and level j

Sum of squares SS_e is calculated by equation 7 [55].

$$SS_e = SS_T - SS_A - SS_B - SS_C - SS_D - SS_E \quad (7)$$

The degree of freedom is computed by equation 8 [55].

$$D_T = N - 1 \quad (8)$$

Degree of freedom for each parameter tested is calculated by equation 9.

$$V_P = SS_P / D_P \quad (9)$$

F-Value is calculated using this relation by equation 10.

$$F_P = \frac{V_P}{V_e} \quad (10)$$

And contribution percentage is calculated using equation 11 [55].

$$\rho_P = \frac{SS_P}{SS_T} \quad (11)$$

3.10 Response Surface Methodology

Response Surface Methodology (RSM) constitutes a set of mathematical approaches focused on fitting a polynomial relation to experimental data. The primary objective is to predict the behavior of processes and improve the levels of independent variables to achieve the optimal levels of dependent variables [56],[57].

This study utilizes Response Surface Methodology (RSM) to construct predictive models for erosion wear observed in the samples. Three input variables, namely the concentration of the slurry, design, and impingement angle, are taken into consideration. The impact of these variables is illustrated through contour plots, providing a visual representation of their effects on erosion wear in the samples.

3.11 Summary

This chapter provides a detailed overview of the experimental apparatus and techniques used for sample preparation. It includes comprehensive details about the conditions for sample preparation

and experimentation. The section also discusses various measurement methods, including their application in quantifying the extent of erosion in PLA samples resulting from multiphase flow, as well as the quantification of erosion and degradation outcomes within the PLA samples.

Additionally, the chapter introduces the design of experiments, outlining the sequence in which the tests were conducted and providing insights into the input and output parameters utilized in the L9 Taguchi array. It explains the use of ANOVA for ranking parameters based on their significance and details the methodology for determining the contribution percentage of each parameter. Moreover, the presentation of experimental results employs Response Surface Methodology (RSM) in the form of contour plots to enhance understanding.

CHAPTER 4 : RESULTS AND DISCUSSION

4.1 Introduction

This chapter elaborates on the results obtained from the methodology described in Chapter 3, focusing on experimental findings related to solid particle erosion under liquid-sand and liquid-sand-air conditions. A detailed analysis, encompassing both quantitative and qualitative aspects, is provided, including discussions on erosion and degradation rates, surface coverage by the erodent's, and measurements such as thickness and mass assessments of the samples. Microscopic techniques like Scanning Electron Microscopy (SEM) are used to complement these quantitative measurements, and the ImageJ software is employed to evaluate the area covered by the eroded surface. Furthermore, the chapter explores the resistance of different morphological surfaces, highlighting the optimal design for erosion mitigation. It also delves into collateral damage induced by erodent's, providing insights into the performance of PLA in various environments. The results and discussion shed light on the erosion induced by liquid-sand and liquid-sand-air flow on PLA, with SEM imagery elucidating the microscopic mechanisms occurring on the material surface. Additionally, 3D scanned samples are used to calculate thickness post-experimentation, offering information on PLA expansion and depth wear. Taguchi ANOVA is applied to the results to figure out the most significant conditions for minimizing erosive wear, and the chapter concludes with the presentation of experiment results through contour plots, effectively illustrating the effect of input parameters on the output parameters.

4.2 Thickness and Mass Loss Measurements

Thickness and mass were measured using a micrometer and a gravimetric balance with the least count. However, only thickness loss was considered as the chosen output parameter, as mass loss measurements were excluded due to the presence of erodent particles embedded onto the sample surfaces post-testing, which added additional weight from the worn-out sample and erodent's. Polymeric materials produced using injection molding processes can absorb water despite being void less and completely solid [58], [59]. In contrast, samples manufactured using 3D printing technology have a higher capacity for water absorption due to the presence of more pores/voids [60]. During experimentation, all samples gained some water weight, increasing their total mass. To account for this, the specimens were dried in a vacuum furnace for 1 hour at 50°C and then cooled in air, following the procedures from previous research [61]. It was anticipated that there

would be a substantial reduction in the mass of specimens due to the deformations attributed to the liquid-sand flow on the surface of PLA samples. While an increase in the weight of samples was observed, it did not accurately reflect the exact weight due to some particles adhering to the surface, thereby increasing the total weight. It was challenging to assess the overall weight loss of the samples experimentally due to the number of particles embedded on the surface, so in this study, they are presented as net weight gain, which is the sum of the number of particles embedded onto the surface of the sample and the mass of the sample after experimentation. Determining mass loss by removing penetrated erodent's was found to be impractical. Thickness reduction measurements using a micrometer indicate liquid-sand and liquid-sand-air flow contributed to the thickness reduction of PLA samples. Thickness and mass measurements of liquid-sand and liquid-sand-air are discussed separately, but before studying them, it is important to understand the effect of different input parameters.

4.3 Effect of Input parameters

4.3.1 Effect of Erodent size

Erosion is influenced by characteristics of the erodent, including its dimensions, form, and hardness [42]. A solid-liquid slurry was created by using natural silica sand with a nominal size of 300 μm, combined with tap water as the erodent. The microscopic depiction of the rodent is presented in Figure 3. Examination of the image reveals a unique pattern where the particles exhibit a consistent and block-like structure.

4.3.2 Effect of Surface Morphology

The decline in erosive wear is also affected by surface morphology. It is recognized as the most influential factor in this research. Various morphologies, including flat, groove, and square groove, were employed for experimentation. It was found that groove is most erosion resistant and this is because the said design reduces direct impact of velocity. The lower speed of velocity results in the minimum erosion, similarly square groove observed moderate erosion. While maximum erosion was observed in flats, this is because the rodents continuously strike on the surface leading to maximum erosion.

4.3.3 Effect of Impact Angle

Experiments were conducted on three different angles 60º, 75º and 90º. When the angle was 90 degrees, the erodent particles impact the surface with the highest velocity component

perpendicular to the surface. This results in the maximum kinetic energy being transferred to the material, leading to the highest erosion rate.

At 75 degrees, the velocity component of the erodent particles is still relatively high, but it is not as effectively directed perpendicular to the surface as at 90 degrees. This results in a moderate transfer of kinetic energy to the material, leading to a moderate erosion rate.

When the angle is 60 degrees, the velocity component of the erodent particles is the least effective in transferring kinetic energy to the material, as a significant portion of the velocity is directed parallel to the surface rather than perpendicular. This results in the minimum erosion rate.

4.4 Thickness and Mass loss measurements for Liquid-Sand Flow:

4.4.1 Thickness Reduction Evaluation

Thickness losses were calculated from the specimens as shown in Figure 4 Micrometer screw gauge measurements of thickness reduction show that slurry had a role in the PLA samples' thickness reduction. Table 4.1 displays thickness before experiments and after experiments. The findings suggest that R3 exhibited the greatest reduction in thickness, amounting to a loss of 1.761 mm.

The primary factor behind this phenomenon may be the predominance of plastic deformation coupled with micro-cutting and fracture as shown in the zoom portion of R3 in Figure 4.1. The harder particles from the rodent impact the surface with a specific force and angle, leading to micro-cutting and fracture on the surfaces. This, in turn, further enhances the plastic deformation of the surfaces [44]. Similarly zoom portion of R6 and R9 represent material removal and fracture respectively, the reason behind this might be the abrasive particles interacting with the PLA surface, these particles can dig into the material and displace it, leading to the formation of material removal and plough marks.

In contrast, minimum thickness loss was observed in R4. This observation can be explained by the fact that the sample with the lowest concentration of 1 wt.% experienced a reduced number of erodent strikes, leading to minimal thickness loss compared to the other samples. This indicates that the concentration of erodent particles directly influences the erosion behavior, with lower concentrations resulting in less material loss.

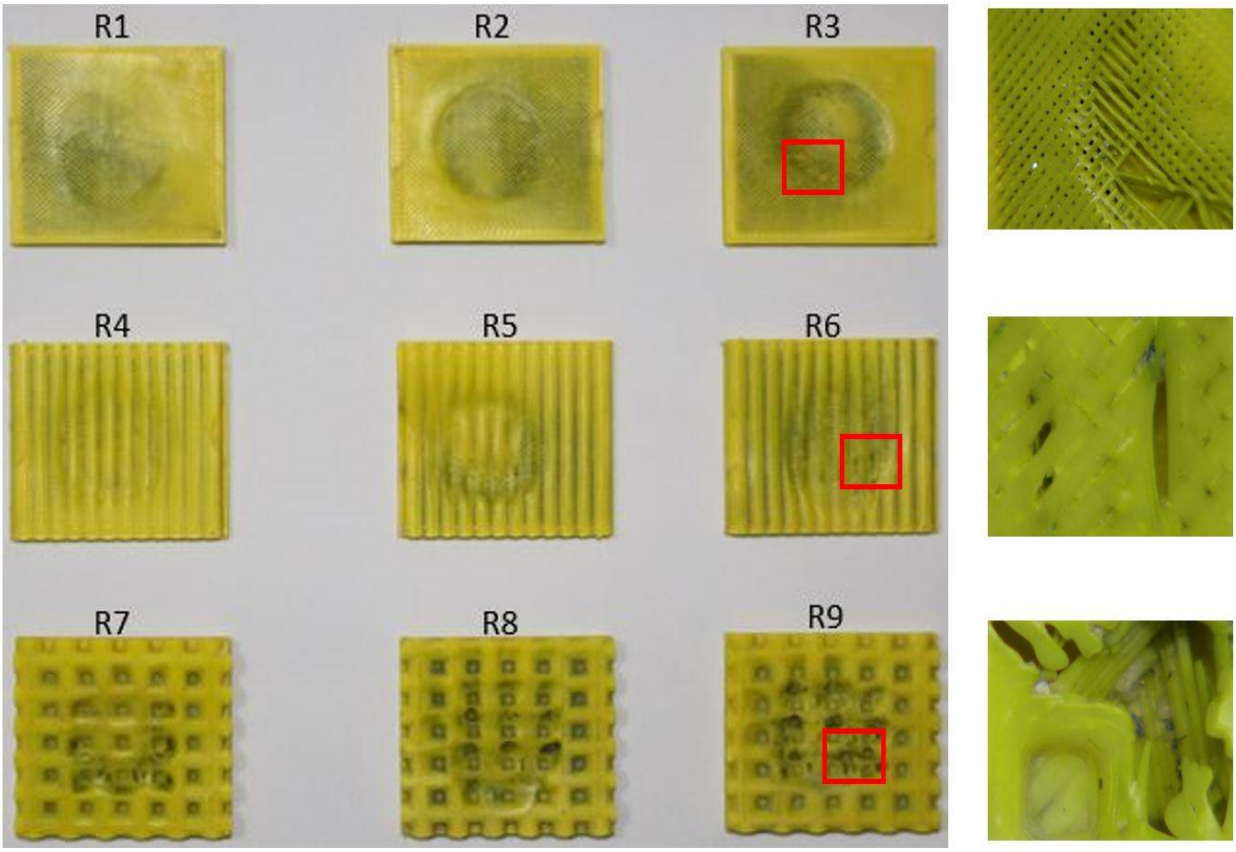

Figure 4.1: Specimens After Performing Experiments.

4.4.2 Weight Gain and Loss Analysis

Polymeric materials produced through injection molding processes have the capacity to absorb water despite their void less and fully solid nature [62], [63]. In contrast, specimens fabricated using 3D printing technology possess a higher potential for water absorption because of the increased number of pores and voids within [64]. During the experimental phase, all samples experienced an increase in weight due to water absorption, consequently raising their total mass. To mitigate the impact of water weight on the specimens, they underwent a drying process in a vacuum furnace for 1.5 hours at 50°C as shown in figure 4.2. Anticipated was a significant reduction in the mass of the samples due to deformations induced by slurry on the surface of PLA samples. Minimum mass loss was observed as compared to thickness loss as shown in Table 4, this minimum mass loss occurred due to embedded particles in the specimens as shown by arrows in Figure 4.2 due to which it was difficult to precisely represent the actual mass loss. Furthermore, in Figure 4.2 the surfaces of R2 and R3 exhibit fractures, while the groove of R5 shows significant

damage. R6 and R7 display cracks on the surface, similarly, R8 and R9 demonstrate extensive material removal.

Table 4.1: Experimental results of water experiments.

EXPERIMENTS OF LIQUID-SAND FLOW											
Texture	**Run No**	**Concentration Wt.%**	**Angle^{o}**	**Initial Thickness (mm)**	**Final Thickness (mm)**	**Thickness loss (mm)**	**% Thickness loss**	**Initial Mass (g)**	**Final Mass (g)**	**Mass Loss (g)**	**% loss in mass**
D1	R1	1	60	3.693	2.726	0.967	26.185	3.545	3.220	0.325	9.168
D1	R2	3	75	3.693	2.356	1.337	36.204	3.545	3.027	0.518	14.612
D1	R3	5	90	3.693	1.932	1.761	47.685	3.545	2.558	0.987	27.842
D2	R4	1	75	3.859	3.159	0.700	18.139	3.935	3.658	0.277	7.039
D2	R5	3	90	3.859	2.735	1.124	29.127	3.935	3.499	0.436	11.080
D2	R6	5	60	3.859	2.643	1.225	31.511	3.935	3.417	0.512	13.164
D3	R7	1	90	4.984	3.895	1.089	21.850	4.541	4.142	0.399	8.787
D3	R8	3	60	4.984	3.882	1.102	22.111	4.541	4.116	0.428	9.360
D3	R9	5	75	4.984	3.531	1.453	29.153	4.541	3.849	0.692	15.239

In this study, the results are presented as a net mass loss, encompassing both the particles embedded on the surface and the mass of the sample post-experimentation. Detailed findings are provided in Table 4.1

The findings presented in Table 4 clearly indicate that sample R3 underwent maximum mass loss of 0.987 mm. The key factor contributing to this phenomenon might be surface morphology of D1 which is a less stable structure than D2 and D3 respectively.

Similarly minimum loss was observed in R4, the cause for this phenomenon could be the development of a more stable structure. as well as minimum concentration of 1% by weight. Due

to changes in design, thickness loss decreases by approximately 24.98% when moving from flat to groove and increases by approximately 19.49% when moving from groove to square groove.

Figure 4.2: Drying sample using vacuum furnace.

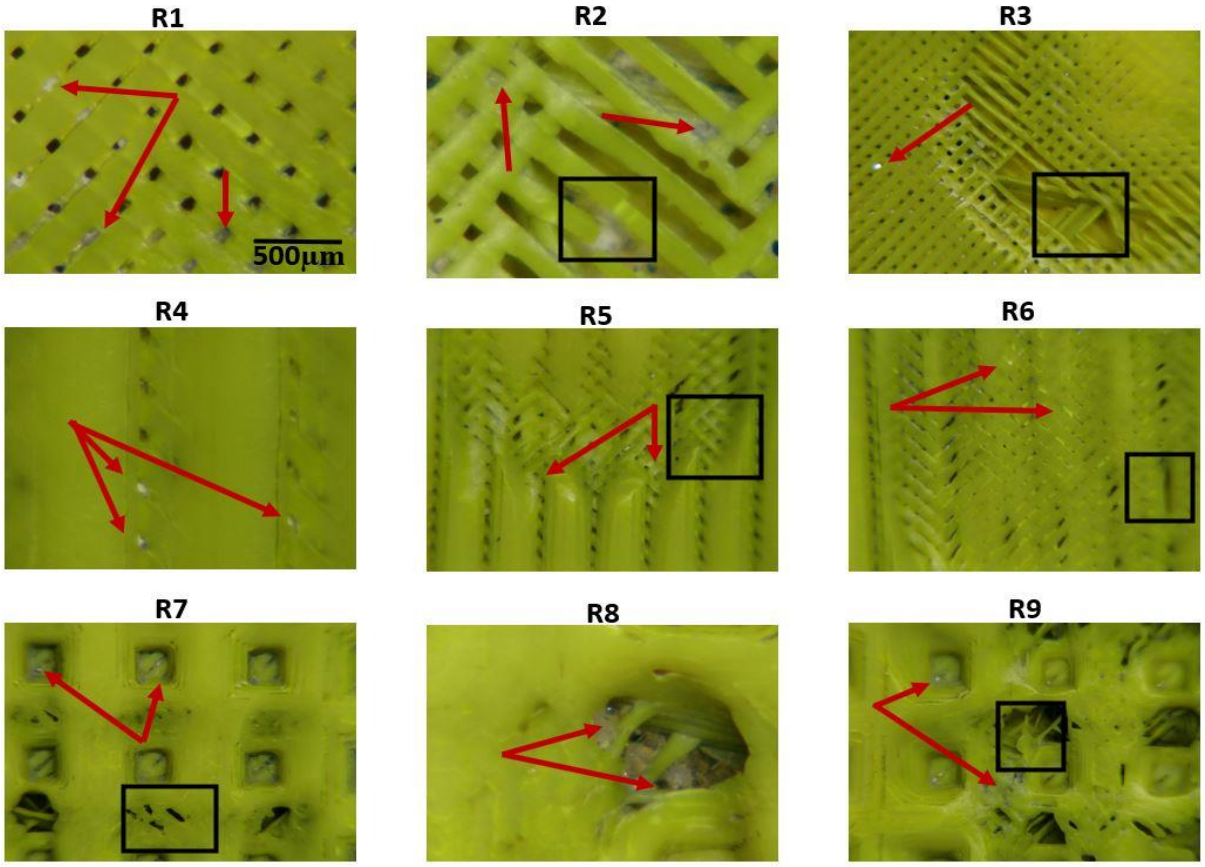

Figure 4.3: Specimens with Embedded Particles

4.5 Macroscopic Analysis for Liquid-Sand Flow

After conducting experiments involving variations in morphology, concentration, and impingement angle, distinctions were observed in the erosion patterns manifested on the surfaces of the samples. Figure 4.4(a), where the impingement angle for R3 was 90º and the concentration was 5% by weight, the presence of cutting and fractures in the eroded region was evident. The hardness and shape of the sand particles could be considered as contributing factors to this phenomenon, coupled with the maximum concentration. The continuous impact of erodent's on the same surface resulted in the removal of material in small particles, leading to cutting and fractures, as depicted in Figure 4.4(a).

Similarly, in the case of R5, 1.124 mm thickness loss was observed. The stability of the surface morphology played a pivotal role, and the 3% concentration also contributed significantly, as the lower concentration resulted in fewer erodent strikes on the specimen.

On the other hand, R3 exhibited maximum erosion, because the effect of kinetic energy on erosion can be significant, especially when considering the incident angle. When the impact angle is 60º, the kinetic energy is distributed over a larger area, potentially resulting in less erosion compared to a more direct impact. At a 90-degree angle, the kinetic energy is concentrated on a smaller area, leading to potentially higher erosion. The primary factor contributing to this occurrence is likely the prevalence of plastic deformation, in conjunction with mechanisms that include micro-cutting and ploughing. Particles with higher hardness from the erodent applied a specific force and angle upon impact, inducing micro-cutting and ploughing effects on the surface. Another contributing factor is the impingement angle, as previous research aligns with the observation that maximum erosion occurs at this angle [65].

3D scanned images of R3, R5 and R9 as shown in Figure 4.4(a) in which R3 show significant depth and thickness loss in the eroded region where 47.685% thickness loss was observed. This could be attributed to the presence of cutting and fractures, as well as plastic deformation, micro-cutting, and ploughing effects on the surface. The combination of a high impingement angle (90º), a high concentration (5% by weight), and the hardness and design of the erodent particles likely resulted in the extraction of material in the form of tiny particles, resulting in cutting and fractures. The extensive erosion evident in R3 indicates that the 3D scanned image shows significant reduction in depth and thickness in the eroded region. The 3D scanned image of R5 shows

moderate depth and thickness loss due to the stability of the surface morphology and the 3% concentration of erodent particles. The lower concentration resulted in fewer erodent strikes on the specimen, which may have led to less severe erosion compared to R3. The 3D scanned image exhibits a moderate level of depth and thickness loss in the eroded region, reflecting the observed 29.127% thickness loss. The 3D scanned image of R9 likely shows substantial depth and 29.153% thickness loss in the eroded region, reflecting the impact of the experimental parameters on the patterns of erosion. The combination of the impingement angle, concentration, and erodent properties likely contributed to the observed erosion, and the 3D scanned image provides visual evidence of the extent of the erosion.

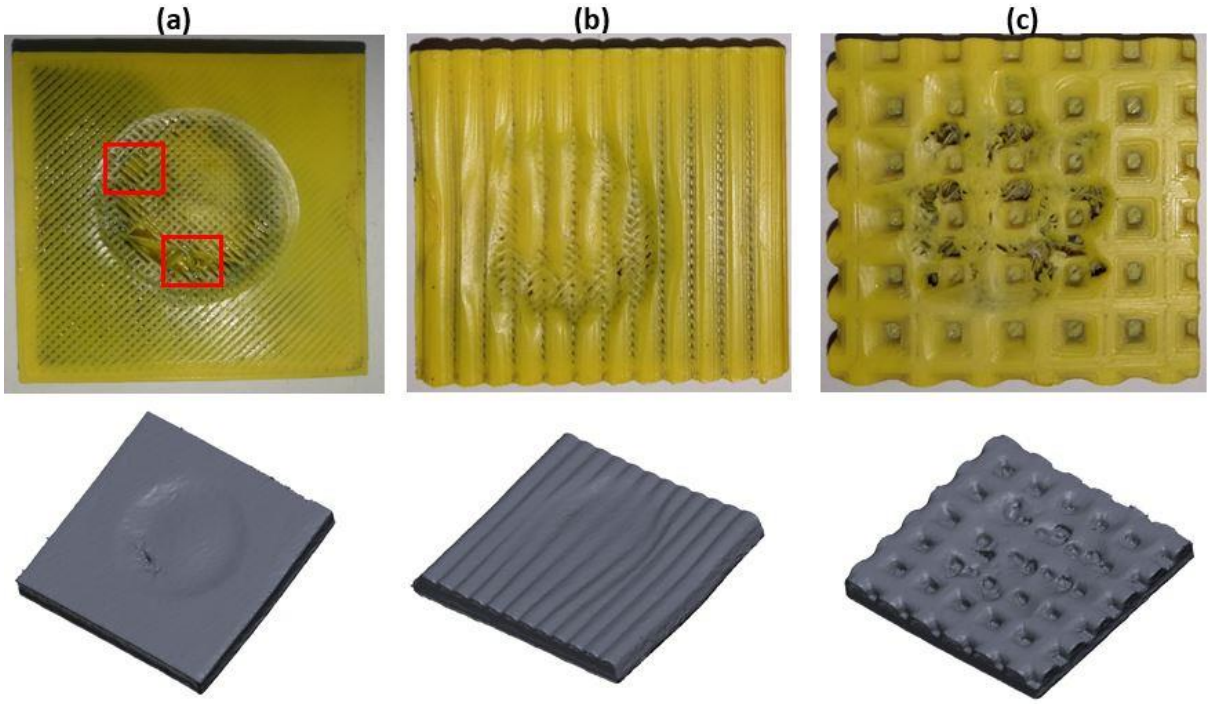

Figure 4.4: Macroscopic & 3D scanned images of worn samples (a) Run 3 (b) Run 5 (c) Run

4.6 Microscopic Analysis for Liquid-Sand Flow

In this investigation, Scanning Electron Microscopy (SEM) was employed to scrutinize the degradation and erosion mechanisms in Polylactic Acid (PLA) samples., emphasizing micro and nano-scale characteristics. The SEM images yielded valuable information about different erosion processes on the sample surface, such as cracks, fractures, ploughing, craters, micro-cutting, and flakes. Figures 4.6, 4.7 illustrate the existence of cracks on the surface of the sample. The cause for these cracks is the low ductility nature inherent in PLA. The crystalline structure of PLA

contributes to its diminished ductility and impact resistance. Upon impact by abrasive particles, concentration of Stress happens at the molecular level, and such concentration may lead to fractures along the planes of fragility within its crystalline structure.

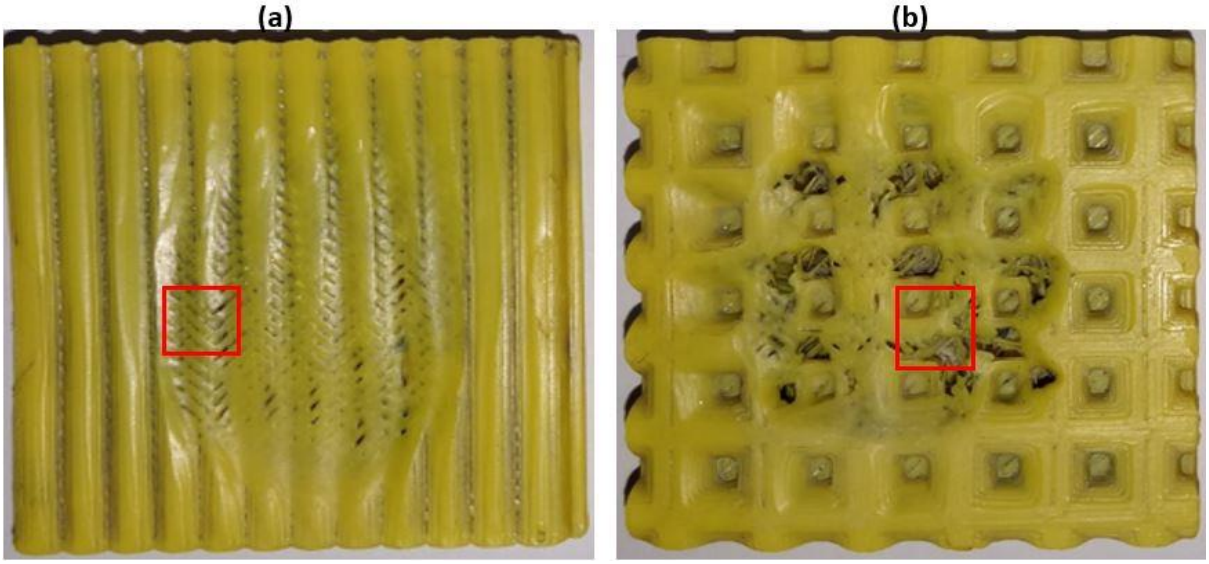

Figure 4.5: Macroscopic image of the worn sample (a) Run 6 (b) Run 9.

Another possible factor contributing to these cracks is the inadequate adhesion between distinct layers of extruded filaments. Formation of uneven surfaces during the extrusion process hinders proper adhesion between layers, resulting in gaps and voids. These gaps may be a potential catalyst for crack formation during sand erosion this finding is observed by [66].

In addition to cracks, the surface of PLA exhibits debris, ploughing, and flakes. The formation of flakes during sand erosion in PLA can be ascribed to many factors. The inherent brittleness of PLA, coupled with the emergence of cracks due to repetitive mechanical stress caused by erodent particles, contributes to the eventual generation of flakes. Furthermore, the crystallinity in PLA plays a pivotal role in flake formation. Crystalline materials often exhibit weaker interfaces between crystalline zones, rendering them more prone to cracks and subsequent flake development [66].

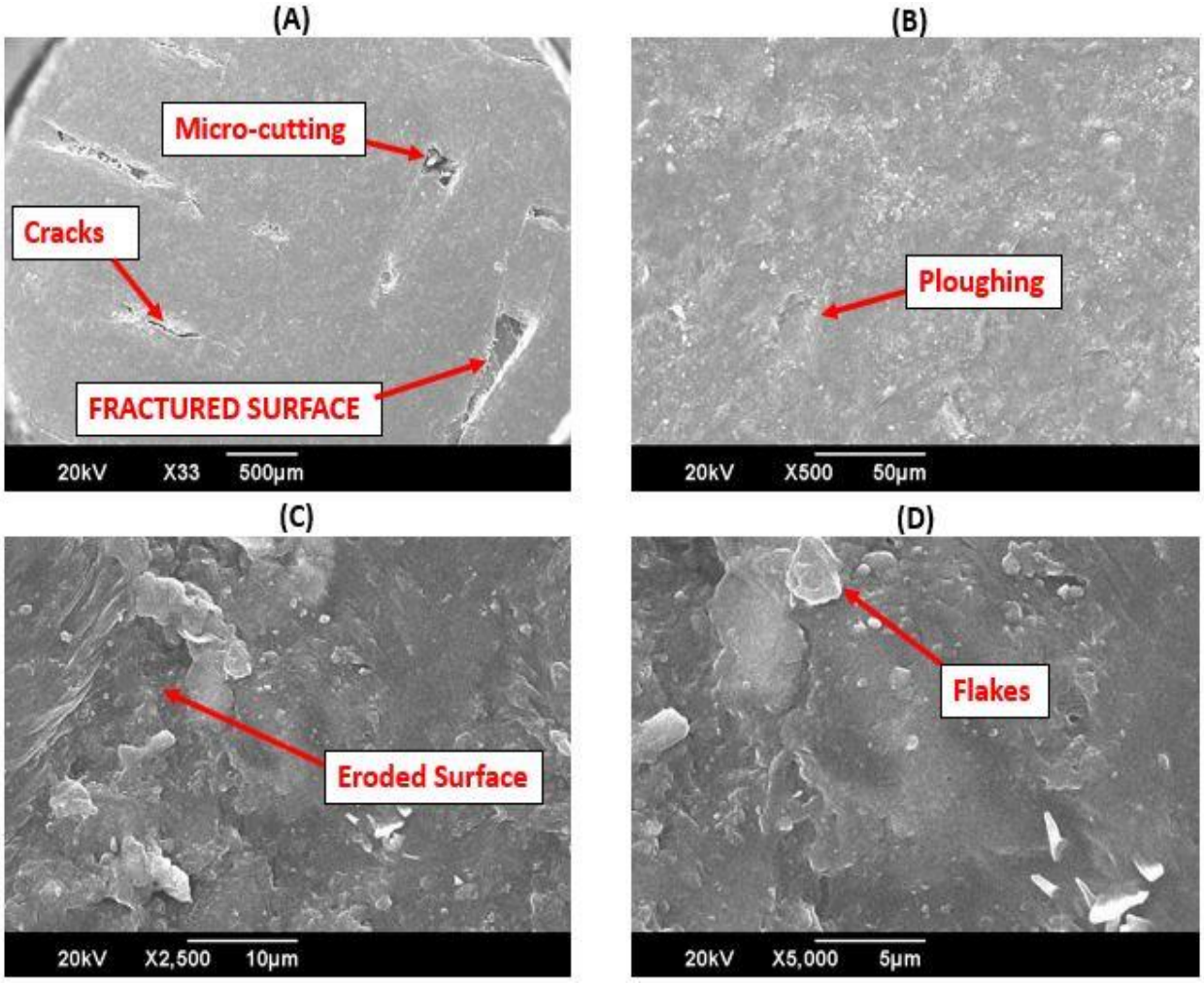

Figure 4.6: Microscopic image of sample S6 for water flow.

Moreover, the size and hardness of erodent particles engaged in the erosion process contribute to micro-cutting. Hard particles are more likely to induce cutting action on the PLA surface, causing micro-scale damage. furthermore, repeated mechanical stress caused by abrasive particles can result in the formation of craters. As these stresses accumulate over time, they can gradually weaken the material, ultimately giving rise to craters because of the material's reaction to the impact. Ploughing can also be a consequence of abrasive particles interacting with the PLA surface. The abrasive particles, propelled by erosive forces, can dig into, and displace material, creating furrows or plough marks.

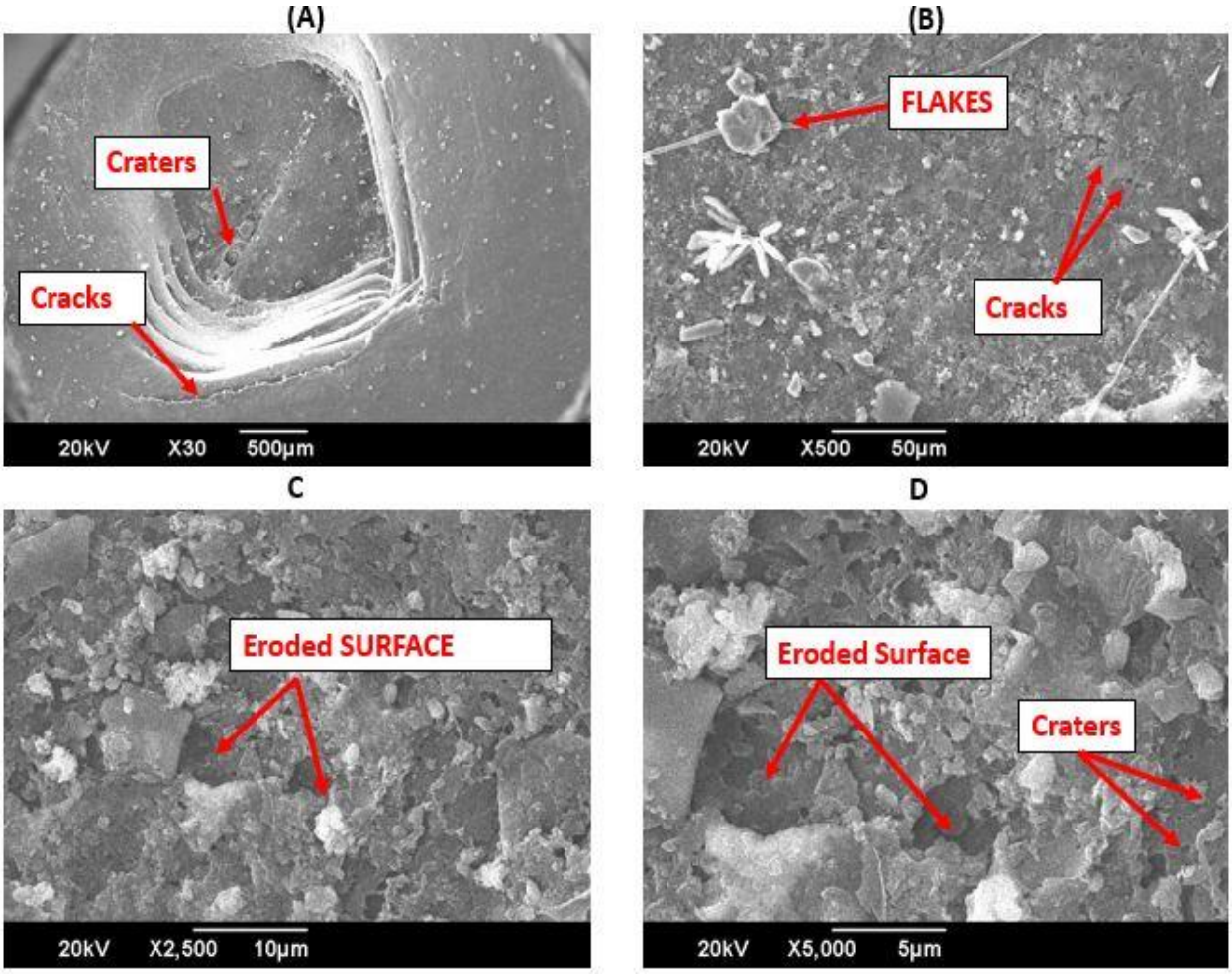

Figure 4.7: Microscopic image of sample S9 for water flow.

4.7 Signal to Noise (S/N) Ratio for liquid-sand:

The signal-to-noise (S/N) ratios for different parameters are computed utilizing the Taguchi L9 orthogonal array. The divergence among S/N ratios is utilized to pinpoint the most significant parameter. These ratios are derived by applying the smaller-is-better quality characteristic, as indicated by equation (3). Table 4.3 displays the experimental results of S/N ratios using Equation (3). Regardless of the quality characteristic, it's noteworthy that a higher S/N ratio implies better quality.

As a result, the process parameter level exhibiting the highest S/N ratio is considered the optimal level.

The experiments revealed a maximum S/N ratio of 3.09804 dB, which was noticed in the 4th Run, showing that the optimal condition corresponds to this run.

The influence of S/N ratios on erosion rate is depicted in Figure 4.8, showing that the lowest erosion wear occurred at design 2 concentration 1 wt.% and angle 60º, while the highest erosion wear was observed at design 1 concentration 5 wt.% and angle 90º. The minimum S/N ratio was identified as -4.91519 and the maximum was 3.09804 dB, respectively. Notably, concentration exhibits a higher delta value, indicating its superior rank among other parameters. Table 4.3 presents the response table, presenting S/N ratios for erosion wear. The values of delta in Table 5 provide insights into the most influential factors, with the most influential parameter having the maximum delta values. Specifically, the delta values are found as 4.1907, 2.4888, and 1.4521 for concentration design and angle respectively.

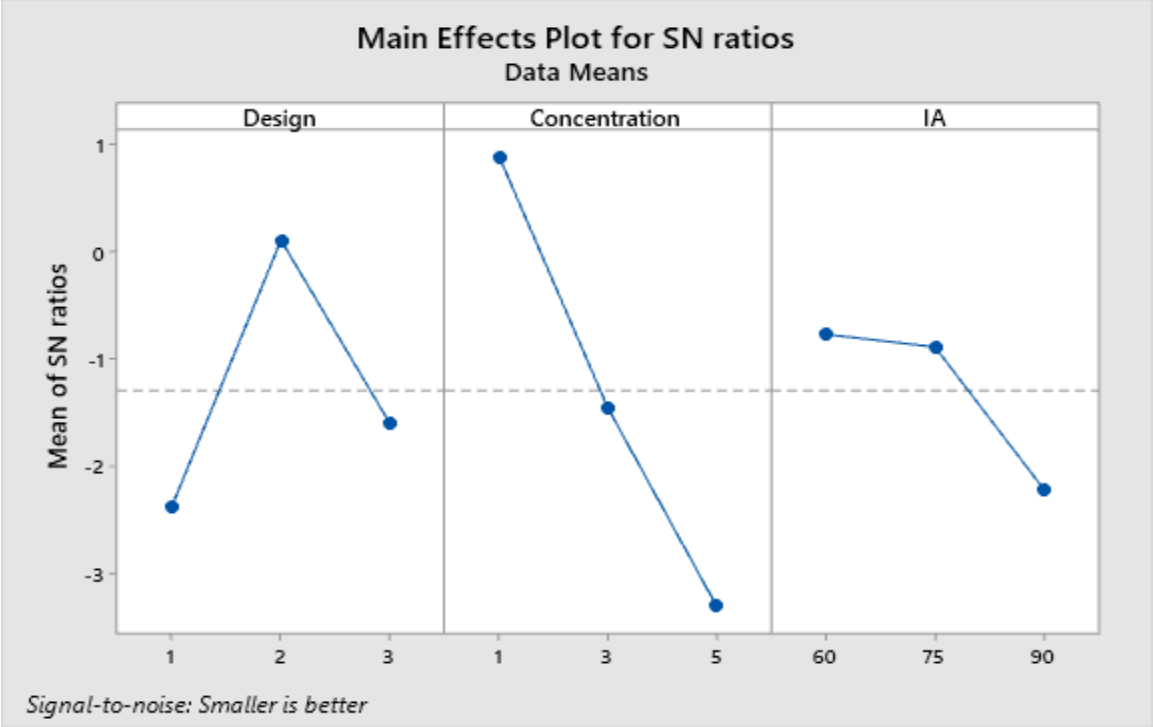

Figure 4.8: Main effect plot of SN ratios for water flow.

Table 4.2: Significance of parameters based on Delta values for water flow.

Level	**Design**	**Concentration**	**IA**
1	-2.3821	0.8830	-0.7716
2	0.1067	-1.4605	-0.8900
3	-1.6098	-3.3077	-2.2237
Delta	2.4888	4.1907	1.4521
Rank	2	1	3

Table 4.3: S/N Ratio based on Taguchi experimental Design for water experiments.

Parameter Level				Experimental Results of Erosion Wear		
Run No	**Design**	**Concentration wt.%**	**Impact Angle^{o}**	**Thickness loss (mm)**	**Mass Loss (g)**	**S/N ratio**
1	D1	1	60	0.967	0.325	0.29147
2	D1	3	75	1.337	0.518	-2.52263
3	D1	5	90	1.761	0.987	-4.91519
4	D2	1	75	0.700	0.277	3.09804
5	D2	3	90	1.124	0.436	-1.01533
6	D2	5	60	1.225	0.512	-1.76272
7	D3	1	90	1.089	0.399	-0.74056
8	D3	3	60	1.102	0.428	-0.84363
9	D3	5	75	1.453	0.692	-3.24531

4.8 Analysis of Variance (ANOVA) and Regression Analysis

ANOVA represents another approach for evaluating the outcomes of erosion wear. It is a statistical tool widely used to evaluate the contribution of each factor in terms of percentage. Based on the findings, under the testing conditions of design 2, concentration 5 and angle 75°, the minimum thickness loss was observed. Figure 4.9 depicts the predominant effect of sole parameters on the erosion process. Design 2 exhibits greater resistance to erosion when compared to both Design 1 and Design 3. The rate of erosion is significantly influenced by concentration, with the erosion rate escalating as the concentration rises from 1 wt.% to 5 wt.%, This occurrence can be ascribed to the escalation in the quantity of erodent, leading to the manifestation of most erosion. Additionally, at the impingement angle of 90°, the maximum thickness loss occurred, while at 60° angle consistently resulted in the least erosion under all conditions, because when the impingement angle is 60º, the kinetic energy is distributed over a larger area, potentially resulting in less erosion compared to a more direct impact.

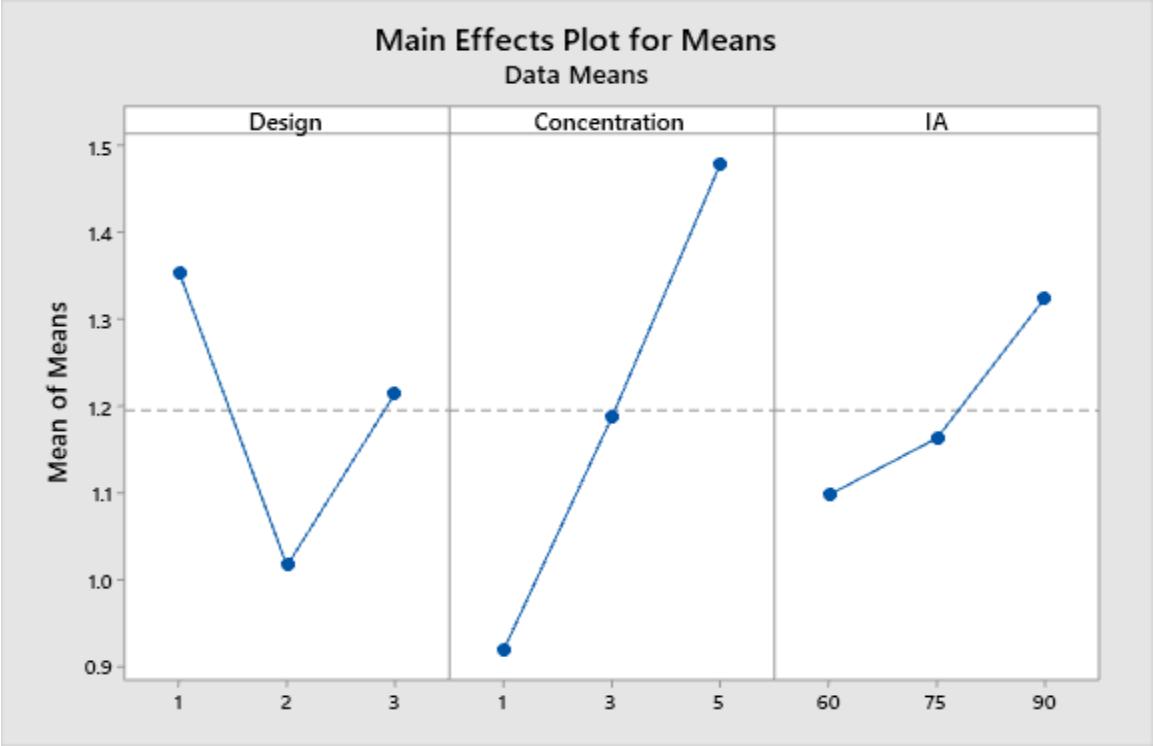

Figure 4.9: Main effect plot for thickness loss for water flow

Regression models have been formulated for the output responses, and the resulting regression equations for D1, D2 and D3 are presented in table 4.4 respectively.

Table 4.4: Regression model of water experiments.

Design			
1	Thickness Loss	=	0.3676 + 0.14025 Concentration + 0.00756 IA
2	Thickness Loss	=	0.0289 + 0.14025 Concentration + 0.00756 IA
3	Thickness Loss	=	0.2273 + 0.14025 Concentration + 0.00756 IA

Table 4.5 illustrates the results of an ANOVA analysis carried out to evaluate the impact of each factor on erosive wear. According to the P-value, each factor exhibits a notable impact on erosive wear. Concentration (64.68%) is identified as the primary contributing factor,

followed by design (23.80%), with the least contributing factor being impact angle (10.56%).

Table 4.5: Contributing parameters of water experiments.

Source	DF	Seq SS	Contribution	Adj SS	Adj MS	F-Value	P-Value
Regression	4	0.722873	99.03%	0.722873	0.180718	102.61	0
Concentration	1	0.472082	64.68%	0.472082	0.472082	268.03	0
IA	1	0.077067	10.56%	0.077067	0.077067	43.76	0.003
Design	2	0.173725	23.80%	0.173725	0.086862	49.32	0.002
Error	4	0.007045	0.97%	0.007045	0.001761		
Total	8	0.729918	100.00%				
SD = 0.0419677, R-Sq = 99.03 %, R-Sq(pred) = 93.73 %							
DF stands for degrees of freedom, SS stands for sum of squares, MS stands for mean squares, F – stands for F value, P stands for P-value, CR stands for contribution ratio %, SD stands for standard deviation; R-Sq. (pred) stands for predicted R^2.							

Figure 4.10 displays a contour plot of thickness loss at varying concentrations and impact angles (IA), as we increase concentration from 1 wt.% to 5 wt.% the thickness loss increases, similar trend was observed as we increased the impact angle from 60° to 90°

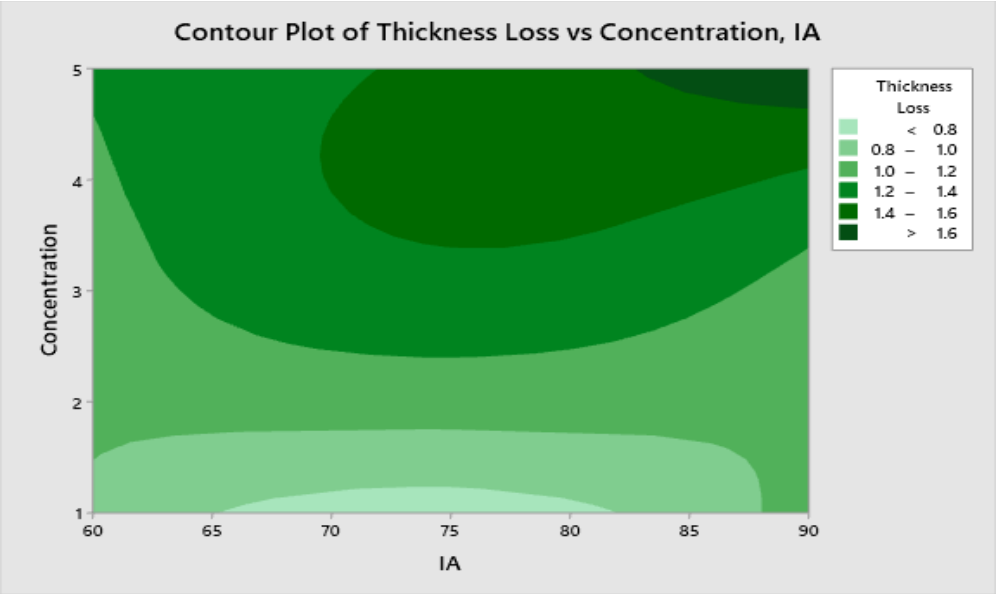

Figure 4.10: Contour plot of thickness loss for water flow.

4.9 Area covered by erosion for liquid-sand flow.

Following the experimentation, the analysis of eroded areas was conducted using Image J software, as illustrated in Figure 4.11. The results revealed that the eroded area was significantly influenced by two key factors: impact angle and erodent concentration. At a 60-degree angle, three tests were conducted, and the calculated average eroded area was 361.799 mm², indicating the minimum coverage. This is attributed to less efficient and shallower impact forces, where the kinetic energy of erosive particles is not effectively transferred to the surface due to the parallel impact, resulting in limited energy transfer and dispersion of erosion material. Moving to a 75-degree angle, the average eroded area increased to 373.266 mm², signifying moderate coverage. Here, the forces become more focused and balanced, leading to efficient kinetic energy transfer and displacement of material. Remarkably, at a 90-degree angle, the maximum eroded area of 435.862 mm² was observed. The perpendicular impact angle allows for optimal kinetic energy transfer, concentrated erosion forces, and efficient material displacement, resulting in the observed maximum coverage in erosion processes. These findings underscore the critical role of erosion angles in influencing the outcomes of erosion experiments.

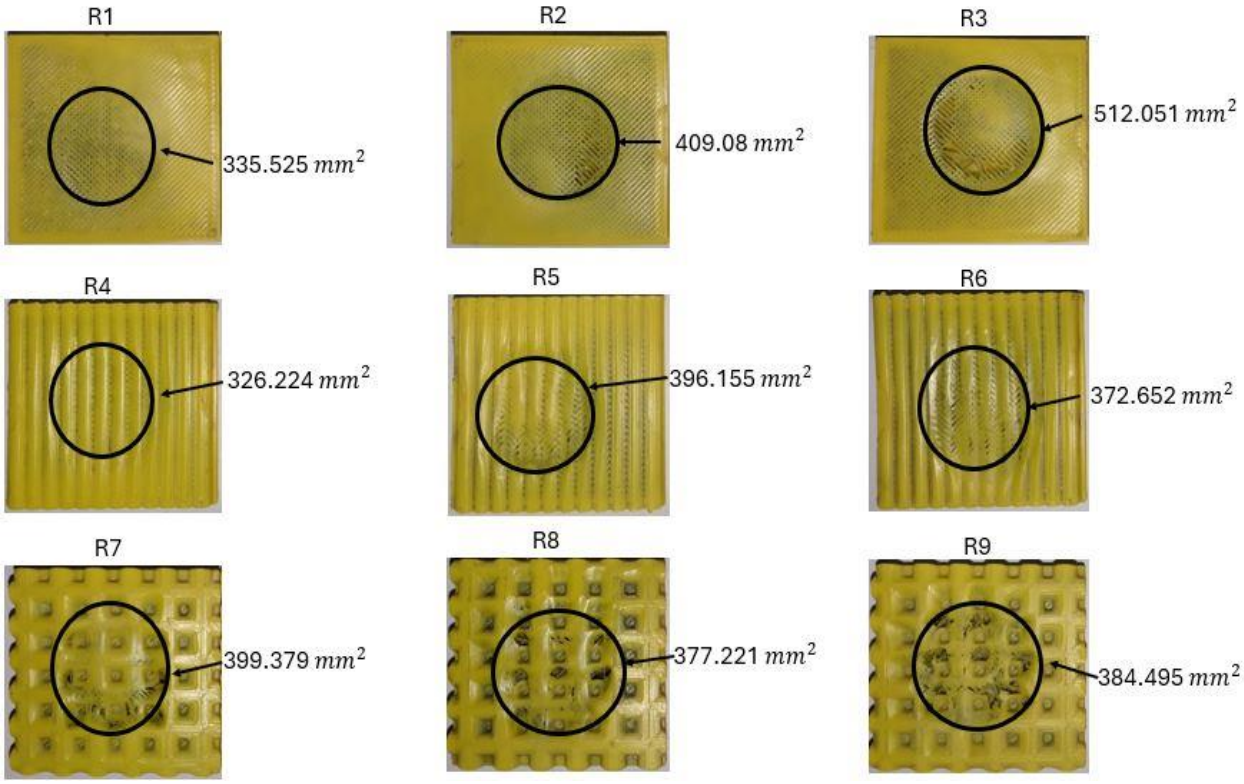

Figure 4.11: Area covered by erosion for water flow.

Table 4.6: Erosion area and pixels covered by samples of water flow.

Conversion factor= 6.20 pixels=1 mm		
Run No	Area covered mm²	Pixels covered
R1	335.525	2080.255
R2	409.08	2536.296
R3	512.051	3174.716
R4	326.224	2022.589
R5	396.155	2455.2
R6	372.652	2310.442
R7	399.379	2476.15
R8	377.221	2338.77
R9	384.495	2383.869

4.10 Thickness Reduction Evaluation for Liquid-Sand-Air Flow

Thickness reductions were determined from the specimens, as depicted in Figure 4. Measurements using a micrometer screw gauge revealed that the slurry played a role in reducing the thickness of the PLA samples. Table 4.7 presents the thickness before and after the experiments. The results indicate that R3 experienced the most significant thickness reduction, with a loss of 1.466 mm.

This occurrence may be primarily attributed to the prevalence of plastic deformation, along with micro-cutting and fractures, as illustrated in the R3 in Figure 4.12. The harder particles from the erodent exerted specific force and angle on the surface, leading to micro-cutting and fractures. This, in turn, further accentuated the plastic deformation of the surfaces. Additionally, the zoomed-in sections of R6 and R9 show material removal and fractures, respectively. This could be due to abrasive particles interacting with the PLA surface, digging into the material, and displacing it, resulting in material removal and plough marks.

In contrast, R4 exhibited minimal thickness loss. This can be explained by the fact that the sample with the lowest concentration of 1 wt.% experienced fewer erodent strikes, resulting in minimal thickness loss compared to the other samples. This indicates that the concentration of erodent

particles directly influences erosion behavior, with lower concentrations leading to less material loss.

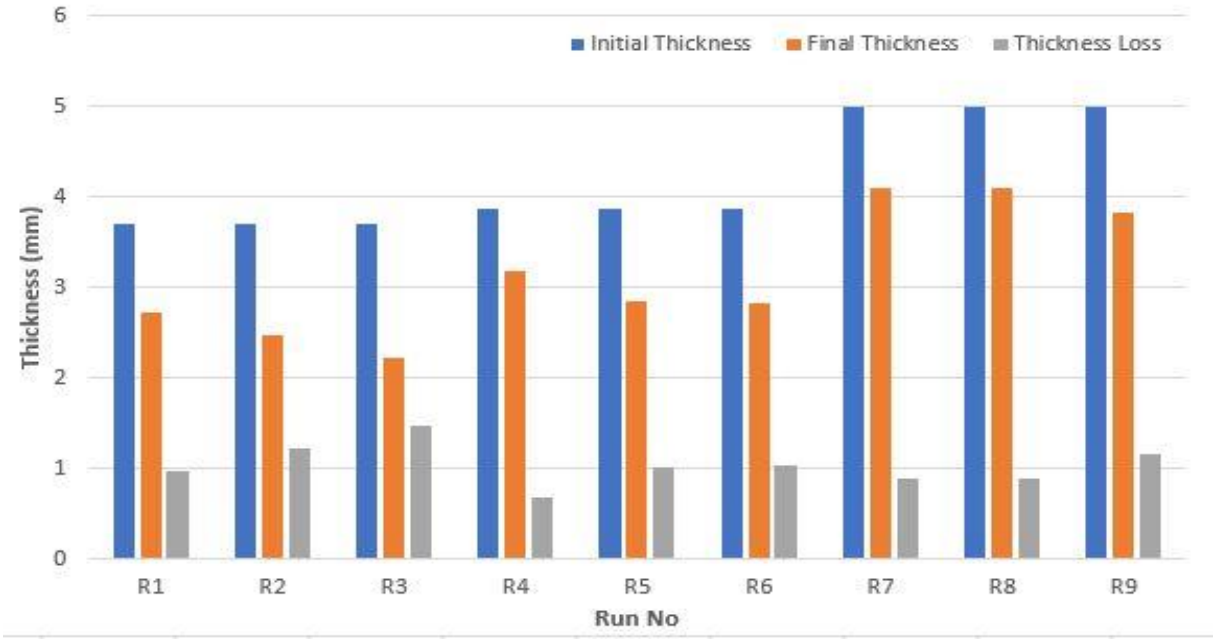

Figure 4.12: comparison of thickness before and after experimentation.

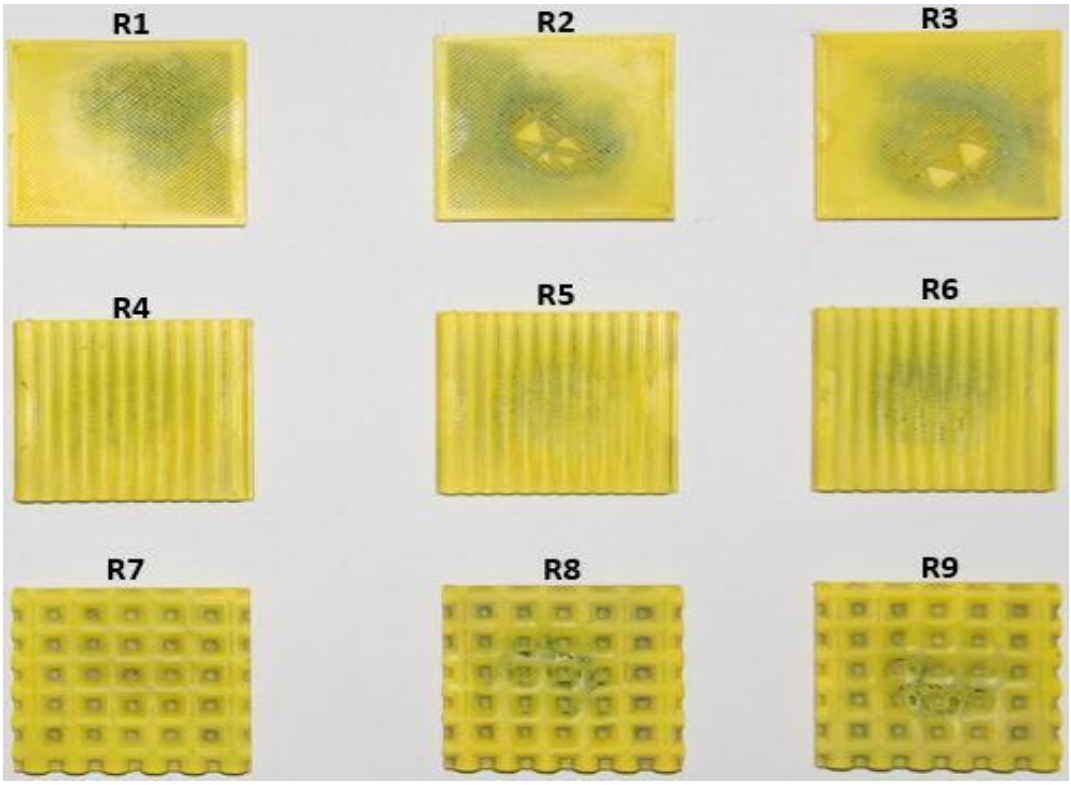

Figure 4.13: Specimens after experimentation.

Table 4.7: Experimental results of Air flow.

EXPERIMENTS OF AIR FLOW											
Texture	**Run No**	**Concentration Wt. %**	**Angle^{o}**	**Initial Thickness (mm)**	**Final Thickness (mm)**	**Thickness loss (mm)**	**% Thickness loss**	**Initial Mass (g)**	**Final Mass (g)**	**Mass Loss (g)**	**% loss in mass**
D1	R1	1	60	3.693	2.730	0.963	26.076	3.545	3.002	0.543	15.317
D1	R2	3	75	3.693	2.481	1.212	32.827	3.545	2.633	0.912	25.726
D1	R3	5	90	3.693	2.227	1.466	39.697	3.545	2.344	1.201	33.879
D2	R4	1	75	3.859	3.171	0.688	17.828	3.935	3.529	0.406	10.318
D2	R5	3	90	3.859	2.853	1.006	26.069	3.935	3.073	0.862	21.906
D2	R6	5	60	3.859	2.834	1.025	26.561	3.935	3.060	0.875	22.236
D3	R7	1	90	4.984	4.090	0.894	17.937	4.541	4.040	0.501	11.033
D3	R8	3	60	4.984	4.095	0.889	17.837	4.541	4.041	0.500	11.011
D3	R9	5	75	4.984	3.831	1.153	23.134	4.541	3.658	0.883	19.455

4.11 Weight Gain and Loss Analysis for Liquid-Sand-Air Flow

Polymeric materials manufactured through injection molding processes can absorb water despite being void less and fully solid in natures [63]. Conversely, specimens created using 3D printing technology have a higher propensity for water absorption due to the increased number of pores and voids within them [64]. During the experimental phase, all samples gained weight because of water absorption as shown in figure 4.14, leading to an overall increase in their weight. To counteract the influence of water weight on the specimens, they underwent a drying process in a vacuum furnace for 1.5 hours at 50°C. It was expected that the weight of the samples would significantly decrease due to deformations caused by the slurry on the surface of the PLA samples. However, minimal weight loss was observed compared to thickness loss, as indicated in figure. This minimal mass loss occurred due to embedded particles in the specimens, making it difficult to accurately represent the actual weight loss.

In this study, the results are presented as a net weight loss, encompassing both the particles embedded on the surface and the weight of the sample after experimentation. Detailed findings are provided in Figure 4.14.

The results presented in figure 4.14 clearly indicate that sample R3 experienced the maximum weight loss of 33.879%. The primary factor contributing to this phenomenon might be the surface morphology of D1, which is a less stable structure compared to D2 and D3, respectively.

Similarly, the minimum loss was observed in R4. The cause for this phenomenon could be the development of a more stable structure, as well as a minimum concentration of 1% by weight. Due to changes in design, thickness loss decreases by approximately 28.54% when moving from flat to groove and increases by approximately 16.39% when moving from groove to square groove.

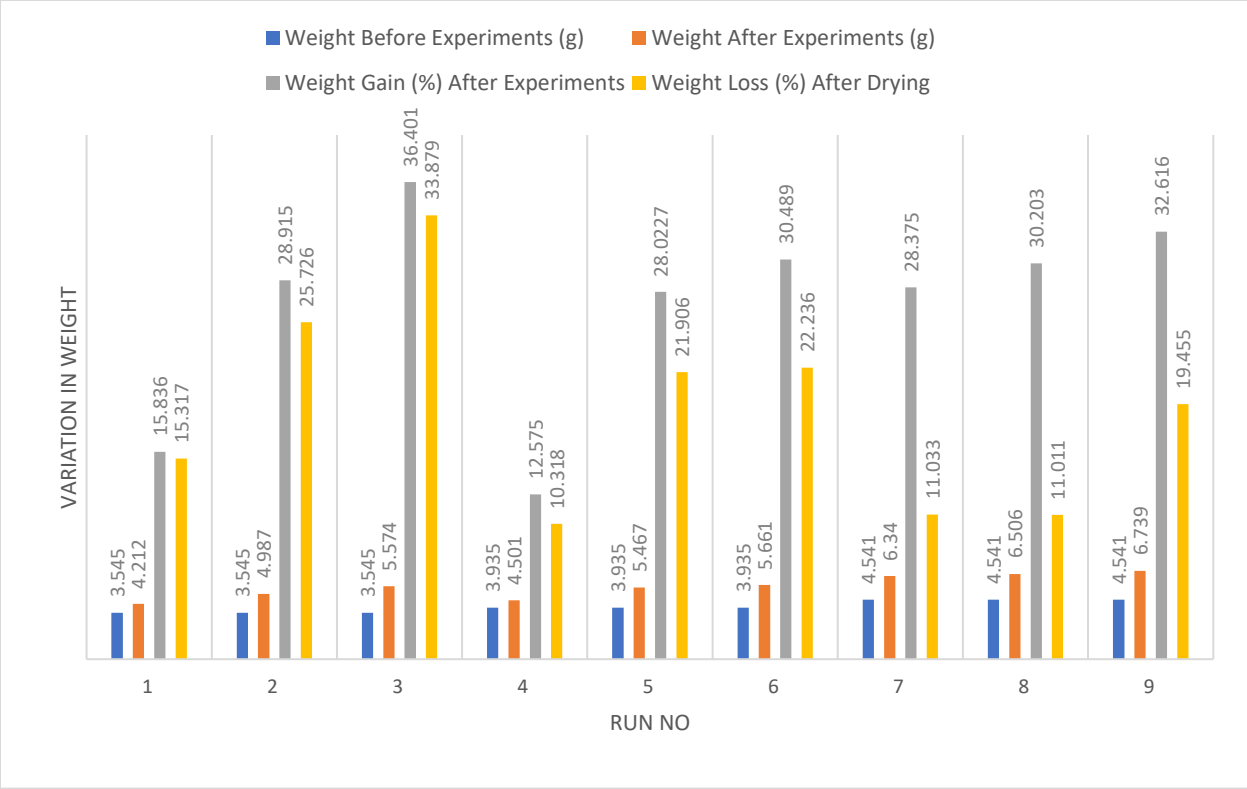

Figure 4.14: Comparison of weight before and after experimentation.

4.12 Macroscopic Analysis

After conducting experiments that involved variations in morphology, concentration, and impingement angle, differences were noted in the erosion patterns seen on the sample surfaces. In Figure 6, where the impingement angle for R3 was 90º and the concentration was 5% by weight,

clear evidence of cutting and fractures in the eroded region was observed. The hardness and shape of the erodent particles, along with the maximum concentration, likely contributed to this phenomenon. The continuous impact of erodent's on the same surface resulted in the removal of material in small particles, leading to cutting and fractures, as shown in Figure 4.14 (a).

Similarly, in the case of R6, a thickness loss of 1.025 mm was observed. The stability of the surface morphology played a crucial role, and the 5% concentration also significantly contributed, as the lower concentration resulted in fewer erodent strikes on the specimen.

On the other hand, R3 exhibited maximum erosion, likely due to the significant effect of kinetic energy on erosion, especially when considering the angle of impact. When the impingement angle is 60º, the kinetic energy is distributed over a larger area, potentially resulting in less erosion compared to a more direct impact. At a 90-degree angle, the kinetic energy is concentrated on a smaller area, leading to potentially higher erosion. The primary factor contributing to this occurrence is likely the prevalence of plastic deformation, in conjunction with mechanisms that include micro-cutting and ploughing.

Particles with higher hardness from the erodent applied a specific force and angle upon impact, inducing micro-cutting and ploughing effects on the surface. Another contributing factor is the impingement angle, as previous research aligns with the observation that maximum erosion occurs at this angle [65].

The 3D scanned images in Figure 6 depict R3, R6, and R9. R3 exhibits significant depth and thickness loss in the eroded region, with a 39.697% thickness loss observed. This can be attributed to cutting, fractures, plastic deformation, micro-cutting, and ploughing effects on the surface, likely due to a high impingement angle (90º), a high concentration (5% by weight), and the hardness and design of the erodent particles. These factors likely led to the extraction of material in the form of tiny particles, resulting in cutting and fractures. The extensive erosion evident in R3 indicates a significant reduction in depth and thickness in the eroded region.

On the other hand, the 3D scanned image of R6 shows moderate depth and thickness loss, likely due to the stability of the surface morphology, potentially leading to less severe erosion compared to R3. The 3D scanned image exhibits a moderate level of depth and thickness loss in the eroded region, reflecting a 26.561% thickness loss.

Likewise, the 3D scanned image of R9 likely shows substantial depth and a 23.134% thickness loss in the eroded region, reflecting the impact of the experimental parameters on the patterns of erosion. The combination of the impingement angle, concentration, and erodent properties likely contributed to the observed erosion, and the 3D scanned image provides visual evidence of the extent of the erosion.

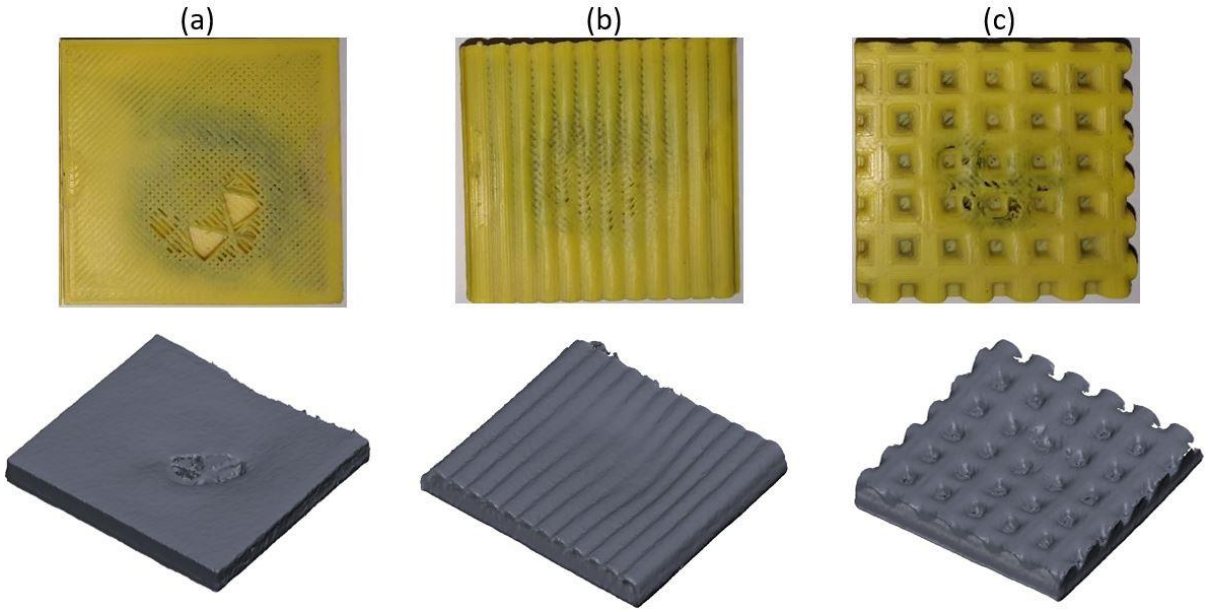

Figure 4.15: Macroscopic & 3D scanned images of worn samples (a) Run 3 (b) Run 6 (c) Run 9 For air flow.

4.13 Microscopic Analysis for Liquid-Sand-Air Flow

This investigation utilized Scanning Electron Microscopy (SEM) to analyze the degradation and erosion mechanisms in Polylactic Acid (PLA) samples at the micro and nanoscale. The SEM images provided valuable insights into various erosion processes on the sample surface, including cracks, fractures, ploughing, craters, micro-cutting, and flakes. Figures 17 and 18 demonstrate the presence of cracks on the sample surface, which can be attributed to the inherent low ductility of PLA. The crystalline structure of PLA contributes to its reduced ductility and impact resistance, leading to stress concentration at the molecular level upon impact by abrasive particles, potentially resulting in fractures within its crystalline structure.

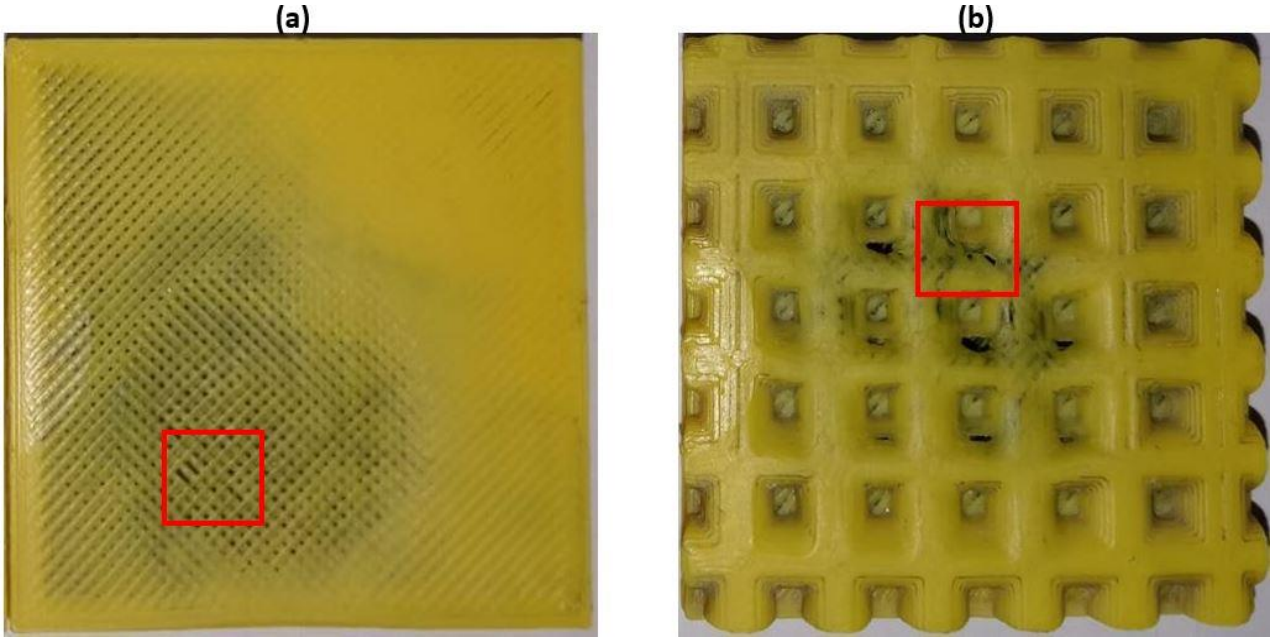

Figure 4.16: Macroscopic image of the worn sample (a) Run 1 (b) Run 9 for Air flow.

Insufficient adhesion between separate layers of extruded filaments could also be a contributing factor to these cracks. The creation of uneven surfaces during the extrusion process impedes the proper bonding between layers, leading to the formation of gaps and voids. These gaps may serve as a potential trigger for crack formation during sand erosion, as noted in this observation by [66].

Apart from cracks, the surface of PLA also shows debris, ploughing, and flakes. The development of flakes during sand erosion in PLA can be ascribed to various factors. The inherent brittleness of PLA, combined with the emergence of cracks due to repeated mechanical stress from erodent particles, contributes to the eventual formation of flakes. Additionally, the crystalline nature of PLA plays a crucial role in flake formation. Crystalline materials frequently exhibit less robust interfaces between their crystalline zones, rendering them more prone to cracking and subsequent flake formation [66].

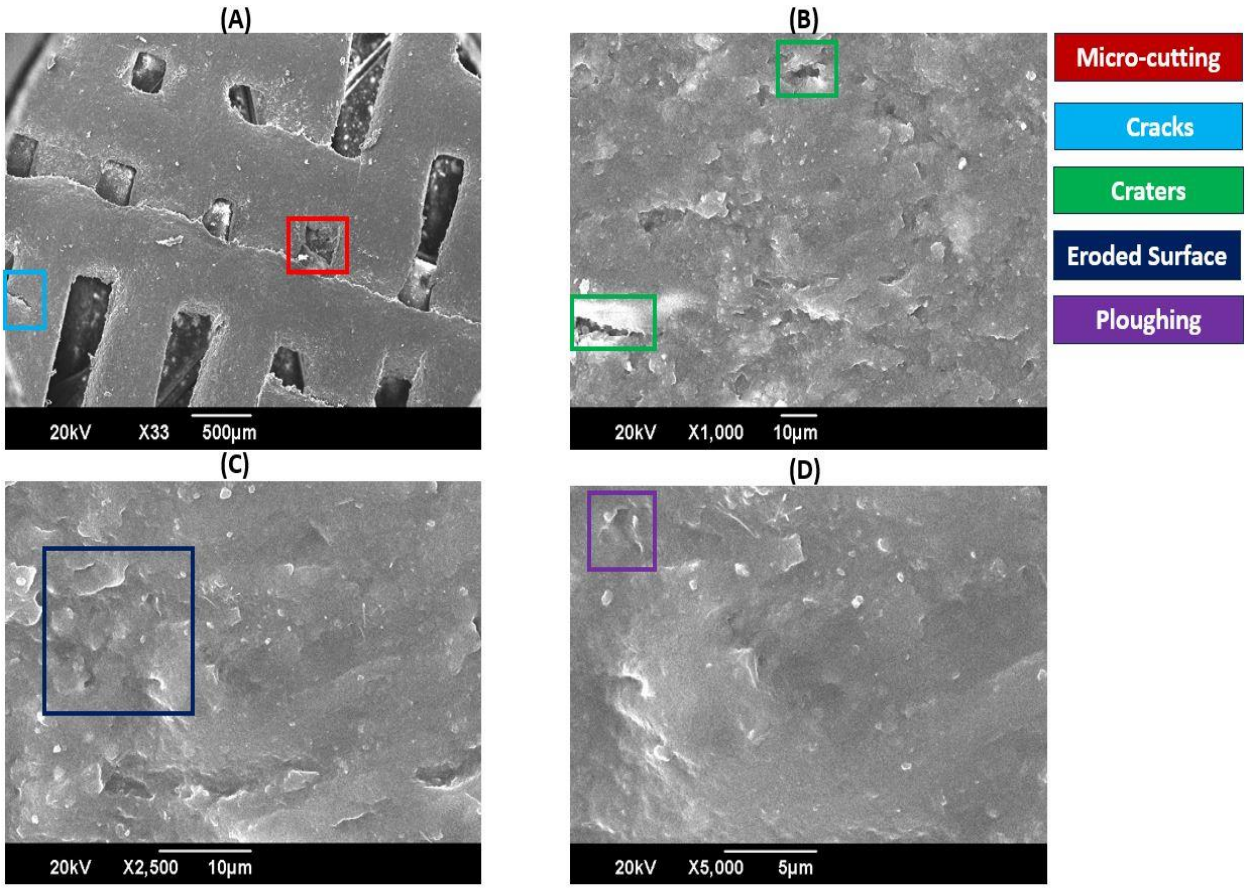

Figure 4.17: Microscopic image of sample S1 for Air flow.

Additionally, the size and hardness of the erodent particles involved in the erosion process contribute to micro-cutting. Hard particles are more likely to cause cutting action on the PLA surface, leading to micro-scale damage. Moreover, repetitive mechanical stress from abrasive particles can lead to the formation of craters. As these stresses accumulate over time, they can gradually weaken the material, ultimately resulting in crater formation due to the material's response to the impact. Ploughing can also occur because of abrasive particles interacting with the PLA surface. Driven by erosive forces, the abrasive particles can dig into and displace material, creating furrows or plough marks.

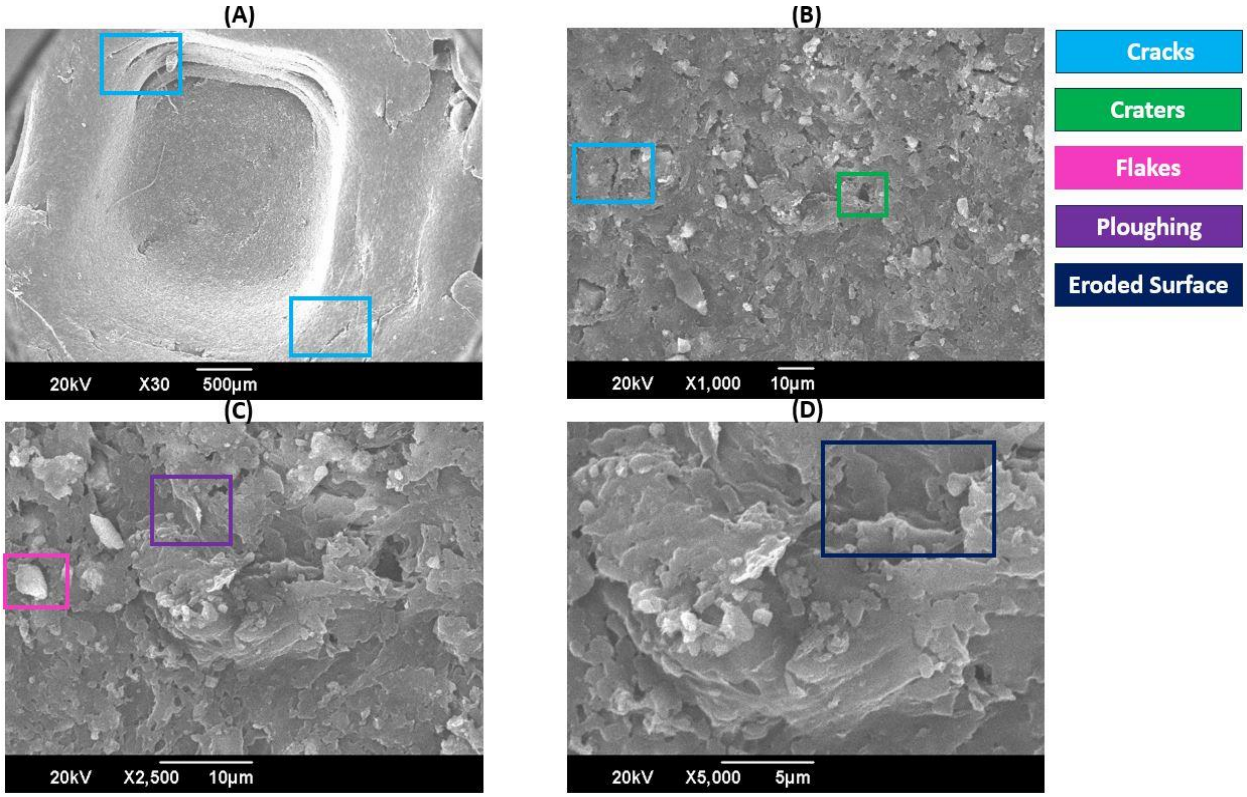

Figure 4.18: Microscopic image of sample S9 for Air flow

4.14 Signal to Noise (S/N) Ratio for Liquid-Sand-Air Flow

The Taguchi L9 orthogonal array is used to calculate the signal-to-noise (S/N) ratios for different parameters. The variation among S/N ratios is utilized to identify the most significant parameter, with these ratios being determined using the smaller-is-better quality characteristic, as illustrated in equation (1) and displayed in Table 4.8. It is important to note that a higher S/N ratio signifies better quality. Therefore, the process parameter level with the highest S/N ratio is considered the optimal level. In the experiments, a maximum S/N ratio of 3.24823 dB was observed in the 4th Run, indicating that this run corresponds to the optimal condition. The impact of S/N ratios on erosion rate is depicted in Figure 4.19, revealing that the lowest erosion wear occurred at design 2 concentration 1 wt.% and angle 75º, while the highest erosion wear was observed at design 1 concentration 5 wt.% and angle 90º. Notably, concentration exhibits a higher delta value, indicating its superior rank among other parameters. The response table in Table 6 presents the S/N ratios for erosion wear, with the delta values providing insights into the most influential factors. Specifically, the delta values are found as 2.4888, 3.1076, and 1.1788 for concentration, design, and angle, respectively.

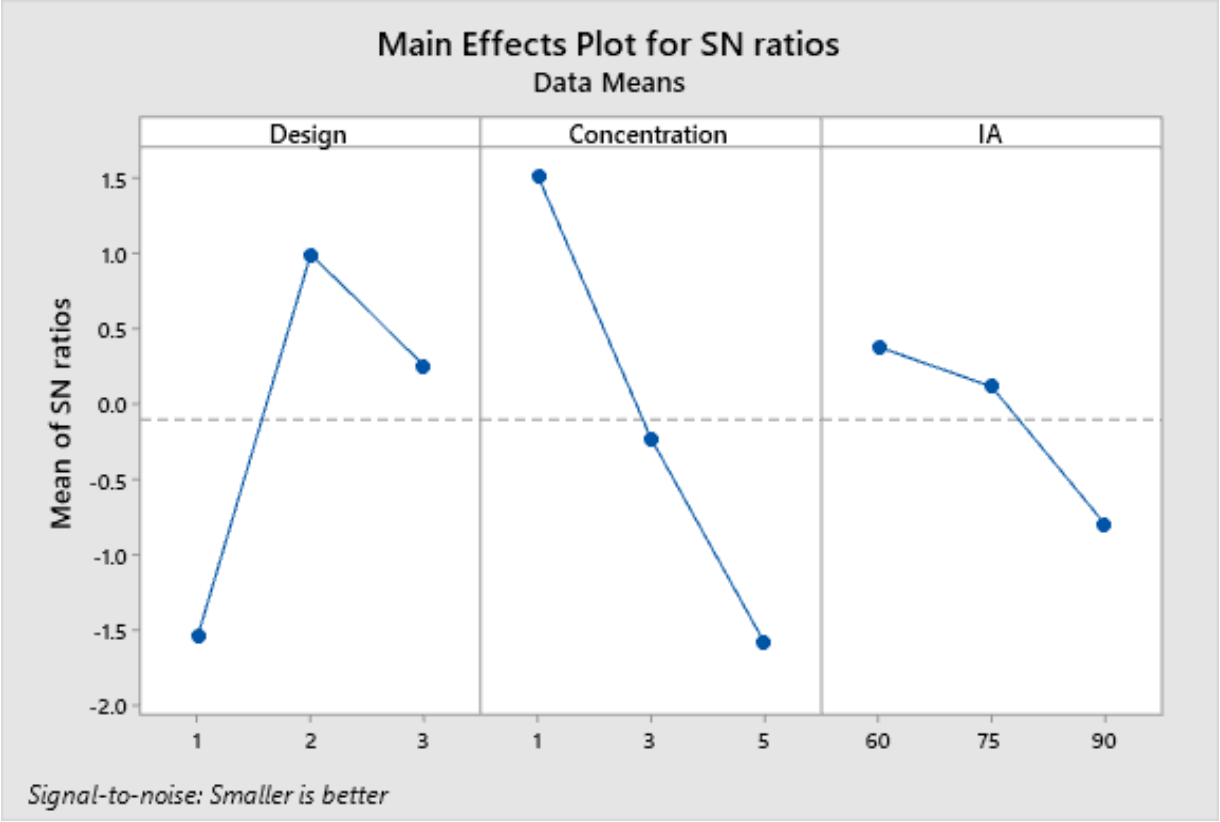

Figure 4.19: Main effect plot of SN ratios for Air flow.

Table 4.8: Significance of parameters based on Delta values for Air flow.

Level	Design	Concentration	IA
1	-1.5551	1.5163	0.3783
2	00.9939	-0.2333	0.1139
3	0.2529	-1.5912	-0.8005
Delta	2.4888	3.1076	1.1788
Rank	2	1	3

Table 4.9: S/N Ratio based on Taguchi experimental Design for water experiments.

Parameter Level				Experimental Results of Erosion Wear		
Run No	**Design**	**Concentration wt.%**	**Impact Angle^{o}**	**Thickness loss (mm)**	**Mass Loss (g)**	**S/N ratio**
1	D1	1	60	0.963	0.543	0.32747
2	D1	3	75	1.212	0.912	-1.67005
3	D1	5	90	1.466	1.201	-3.32268
4	D2	1	75	0.688	0.406	3.24823
5	D2	3	90	1.006	0.862	-0.05196
6	D2	5	60	1.025	0.875	-0.21448
7	D3	1	90	0.894	0.501	0.97325
8	D3	3	60	0.889	0.500	1.02196
9	D3	5	75	1.153	0.883	-1.23659

4.15 Analysis of Variance (ANOVA) and regression analysis for Liquid-Sand-Air Flow

ANOVA offers an alternative method for assessing erosion wear outcomes, serving as a widely used statistical tool for determining the percentage contribution of each factor. The results indicate that, under the testing conditions of design 2, concentration 5, and angle 75°, the minimum thickness loss was observed. Figure 20 illustrates the predominant effect of individual parameters on the erosion process, showing that Design 2 demonstrates greater resistance to erosion compared to both Design 1 and Design 3. The erosion rate is notably influenced by concentration, with the rate increasing as the concentration rises from 1 wt.% to 5 wt.%. This trend is attributed to the greater quantity of erodent, leading to increased erosion. Furthermore, at an impingement angle of 90°, the maximum thickness loss occurred, while a 60° angle consistently resulted in the least erosion under all conditions. This is due to the distribution of kinetic energy over a larger area at a 60^{o} impingement angle, potentially resulting in less erosion compared to a more direct impact.

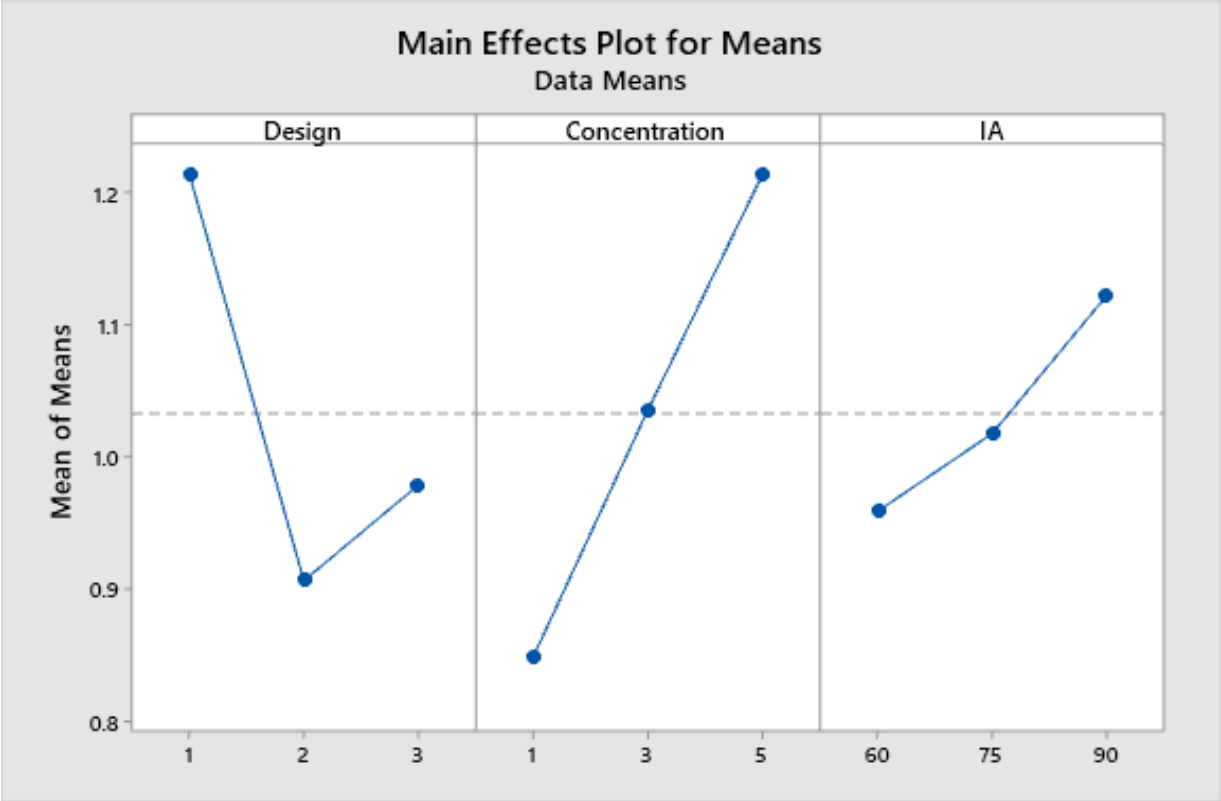

Figure 4.20: Main effect plot for thickness loss for Air flow

Regression models have been formulated for the output responses, and the resulting regression equations for D1, D2 and D3 are presented in Table 4.10 respectively.

Table 4.10: Regression model of thickness loss for Air flow.

Design			
1	Thickness Loss	=	0.5314 + 0.09158 Concentration + 0.005433 IA
2	Thickness Loss	=	0.2241 + 0.09158 Concentration + 0.005433 IA
3	Thickness Loss	=	0.2964 + 0.09158 Concentration + 0.005433 IA

Table 4.11: Contributing parameters of Air experiments.

Source	DF	Seq SS	Contribution	Adj SS	Adj MS	F-Value	P-Value
Regression	4	0.396065	99.34%	0.396065	0.099016	150.01	0
Concentration	1	0.2013	50.49%	0.2013	0.2013	304.96	0
IA	1	0.039854	10.00%	0.039854	0.039854	60.38	0.001
Design	2	0.154911	38.85%	0.154911	0.077455	117.34	0
Error	4	0.00264	0.66%	0.00264	0.00066		
Total	8	0.398705	100.00%				
SD = 0.0256921, R-Sq = 99.34 %, R-Sq(pred) = 96.19 %							
DF stands for degrees of freedom, SS stands for sum of squares, MS stands for mean squares, F – stands for F value, P stands for P-value, CR stands for contribution ratio %, SD stands for standard deviation; R-Sq. (pred) stands for predicted R^2							

Table 4.11 presents the outcomes of an ANOVA analysis conducted to assess the influence of each factor on erosive wear. Based on the P-values, each factor demonstrates a significant impact on erosive wear. Concentration (50.49%) is identified as the primary contributing factor, followed by design (38.85%), with the impact angle being the least contributing factor (10.00%).

Figure 21 exhibits a contour plot of thickness loss at varying concentrations and impact angles (IA). It shows that as the concentration increases from 1 wt.% to 5 wt.%, the thickness loss also increases. A similar trend is observed when the impact angle is increased from 60° to 90°.

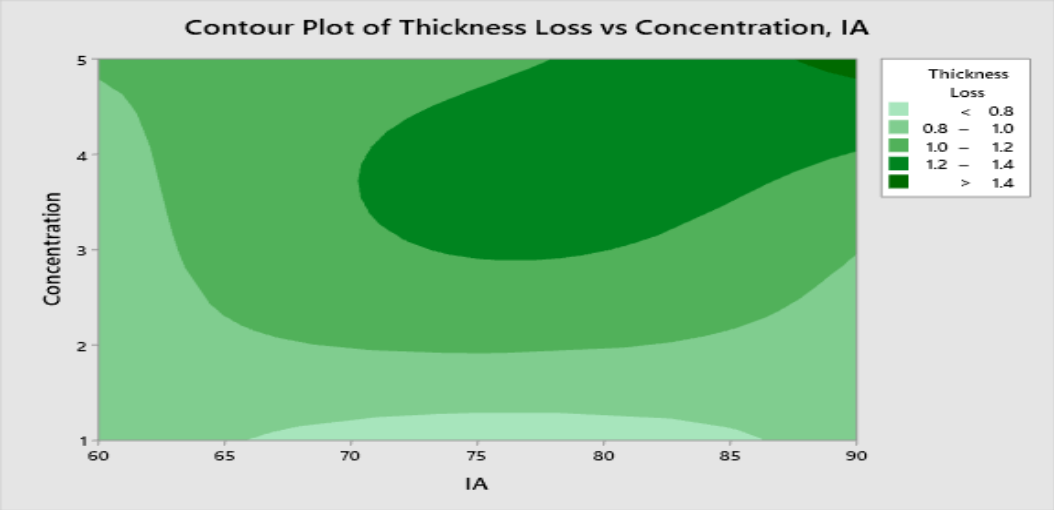

Figure 4.21: Contour plot of thickness loss for Air flow.

4.16 Area covered by erosion for Liquid-Sand-Air Flow

After performing experimentation, the analysis of eroded areas was conducted using Image J software, as illustrated in Figure 4.22. The results revealed that the eroded area was significantly influenced by two key factors: impact angle and erodent concentration. At a 60-degree angle, three tests were conducted, and the calculated average eroded area was 357.255 mm², indicating the minimum coverage. This is attributed to less efficient and shallower impact forces, where the kinetic energy of erosive particles is not effectively transferred to the surface due to the parallel impact, resulting in limited energy transfer and dispersion of erosion material. Moving to a 75-degree angle, the average eroded area increased to 369.393 mm², signifying moderate coverage. Here, the forces become more focused and balanced, leading to efficient kinetic energy transfer and displacement of material. Remarkably, at a 90-degree angle, the maximum eroded area of 438.694 mm² was observed. The perpendicular impact angle allows for optimal kinetic energy transfer, concentrated erosion forces, and efficient material displacement, resulting in the observed maximum coverage in erosion processes. These findings underscore the critical role of erosion angles in influencing the outcomes of erosion experiments.

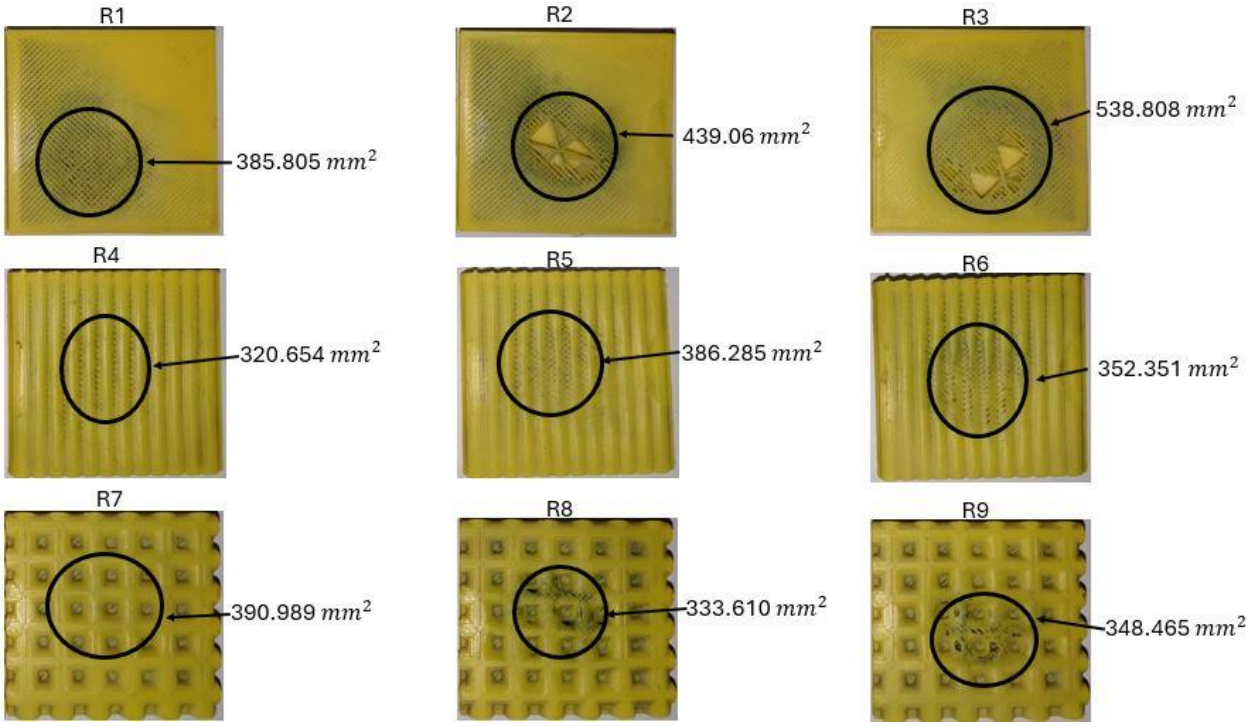

Figure 4.22: Area covered by erosion for Air flow.

Table 4.12: Erosion area and pixels covered by samples of Air flow.

Conversion factor= 6.05 pixels=1 mm		
Run No	Area covered mm^2	Pixels covered
R1	385.805	2334.12
R2	439.06	2656.313
R3	538.808	3259.788
R4	320.654	1939.957
R5	386.285	2337.024
R6	352.351	2131.723
R7	390.989	2365.483
R8	333.61	2018.34
R9	348.465	2108.213

4.17 Summary

In this chapter, a comprehensive examination of the key parameters essential for reducing erosion rates is provided. The assessment primarily focused on thickness loss, as it was impractical to measure mass loss by extracting erodent's from the samples. An interesting observation was made regarding the area covered by erosion which was investigated through Image J software. Additionally, the manifestation of thickness loss was effectively demonstrated through 3-D scanned images, providing valuable insights into the reduction of sample thickness.

The experimentation process involved the use of a specific set of L9 arrays, enabling a systematic investigation. Both macroscopic and microscopic analyses were conducted to gain a thorough understanding of the erosion mechanisms occurring on the sample surfaces. The subsequent application of ANOVA allowed for the determination of the significance associated with each input parameter. The results of this statistical analysis were visually represented through contour plots, serving as a graphical depiction of the research findings.

CHAPTER 5 : RESULTS AND DISCUSSION

This chapter provides a brief explanation of the general findings of the research study. The potential contributions of this research are thoroughly discussed in this chapter. Additionally, the scope of the study and future recommendations are also presented in this chapter.

5.1 Conclusion

This research study investigates sand erosion in Polylactic acid (PLA) samples under solid-liquid and solid-liquid-gas flow conditions. Experimental data was collected from a specially designed and constructed experimental test bench for this specific purpose. To focus exclusively on sand erosion, three different morphologies, namely flat (D1), grooved (D2), and square groove (D3), were employed to assess erosion rates. The erosion test was carried out under solid-liquid and solid-liquid-gas flow at a flow velocity of 6m/s and a particle size of 300 μm. A total of 18 experimental cases were conducted using Taguchi L9 array, with variables including angle (60º, 75º, and 90º), concentration (1 wt.%, 3 wt.%, and 3 wt.%), flow velocity of 6 m/s, and particle size of 300 μm.

In this study, various significant erosion parameters were examined to understand their impact. The research delved into the effects of flow velocity, particle size, Impingement angle and different sand concentration on erosion rate and mechanisms. ANOVA was employed to find out the contribution parameters which affect erosion rate. Additionally, Scanning Electron Microscopy was utilized to analyze the microscopic-level mechanisms of sediment erosion. Furthermore, a hand-held 3D scanner was employed to capture the thickness loss profile both before and after the erosion test.

The significant findings of this research study are thoroughly presented below.

- Design 2 is the preferred option for erosion control, outperforming both Design 1 and Design 3 due to its ability to reduce the direct impact of kinetic energy compared to the other designs. Delta values of concentration, design, and impact angle from the results of the S/N ratio were 4.1907, 2.4888, and 1.4521 for liquid-solid flow and 3.1076,2.4888 and 1.1788 for liquid-solid-gas flow respectively, a higher delta value signifies the most influential parameter. The order of erosion wear influencing parameters is as follows.

Concentration > design > impact angle

- The ANOVA analysis determined the notable contributions of distinct parameters to the erosion rate, with concentration contributing at 64.68%, design at 23.80%, and impact angle contributing at 10.56% for liquid-sand flow similarly concentration contributing 50.49%, design 38.85% and impact angle 10.00% for liquid-sand-gas flow.

- The erosion rate was highest in D1 for a concentration of 5 wt.% and an angle of 90°, while it was lowest in D2 for a concentration of 1 wt.% and an angle of 75°, thickness loss was decreased by approximately 24.98% when the design changed from D1 to D2 and increased by approximately 19.49% when the design changed from D2 to D3 for liquid-sand flow, similarly the thickness loss decreased by around 28.54% when moving from D1 to D2 and increased by approximately 16.39% when moving from D2 to D3 for liquid-sand-gas flow.

- PLA demonstrates a ductile mechanism characterized by features such as craters, micro-cutting, ploughing, and cracks. This behavior is due to the ability of PLA to undergo plastic deformation under stress, allowing it to change shape without breaking. The presence of craters, micro-cutting, ploughing, and cracks indicate that the material can absorb and distribute stress, preventing catastrophic failure.

5.2 Research Contribution

- This study identifies Design 2 as the most effective option for mitigating sand erosion in Polylactic acid (PLA) samples. By employing grooved morphology (D2), which reduces the direct impact of kinetic energy compared to other designs, erosion control is significantly enhanced. This finding offers practical insights for engineers and material scientists aiming to develop erosion-resistant materials or structures, emphasizing the importance of design considerations in minimizing erosion effects.
- Through comprehensive analysis utilizing Scanning Electron Microscopy (SEM), this research elucidates the microscopic-level mechanisms of sand erosion in PLA. By identifying features such as craters, micro-cutting, ploughing, and cracks, the study characterizes PLA's ductile behavior under erosive stress. This understanding of material

response provides valuable knowledge for designing erosion-resistant materials and predicting their performance under varying flow conditions, contributing to the advancement of erosion science and engineering applications.

5.3 Future Recommendations

The research suggests future work to continue advancing this field. Some key recommendations include:

- The erosive wear analysis can be done on elastomers, to understand the wear mechanism in two-phase and three-phase flow.
- The current study was conducted on three different designs which can be enhanced further.
- Adding abrasive particles to water increases its viscosity. Therefore, to better predict sand erosion, it is important to study the impact of viscosity on erosion rates in PLA.

References:

[1] M. Parsi, K. Najmi, F. Najafifard, S. Hassani, B. S. McLaury, and S. A. Shirazi, "A comprehensive review of solid particle erosion modeling for oil and gas wells and pipelines applications," *J Nat Gas Sci Eng*, vol. 21, pp. 850–873, Nov. 2014, doi: 10.1016/j.jngse.2014.10.001.

[2] R. Elemuren, R. Evitts, I. Oguocha, G. Kennell, R. Gerspacher, and A. Odeshi, "Slurry erosion-corrosion of 90° AISI 1018 steel elbow in saturated potash brine containing abrasive silica particles," *Wear*, vol. 410–411, pp. 149–155, Sep. 2018, doi: 10.1016/j.wear.2018.06.010.

[3] N. Ojala *et al.*, "Wear performance of quenched wear resistant steels in abrasive slurry erosion," *Wear*, vol. 354–355, pp. 21–31, May 2016, doi: 10.1016/j.wear.2016.02.019.

[4] R. Macchini, M. S. A. Bradley, and T. Deng, "Influence of particle size, density, particle concentration on bend erosive wear in pneumatic conveyors," *Wear*, vol. 303, no. 1–2, pp. 21–29, Jun. 2013, doi: 10.1016/j.wear.2013.02.014.

[5] J. Aguirre, M. Walczak, and M. Rohwerder, "The mechanism of erosion-corrosion of API X65 steel under turbulent slurry flow: Effect of nominal flow velocity and oxygen content," *Wear*, vol. 438–439, p. 203053, Nov. 2019, doi: 10.1016/j.wear.2019.203053.

[6] Y.-F. Wang and Z.-G. Yang, "Finite element model of erosive wear on ductile and brittle materials," *Wear*, vol. 265, no. 5–6, pp. 871–878, Aug. 2008, doi: 10.1016/j.wear.2008.01.014.

[7] G. Hao, X. Dong, M. Du, Z. Li, and Z. Dou, "A comparative study of ductile and brittle materials due to single angular particle impact," *Wear*, vol. 428–429, pp. 258–271, Jun. 2019, doi: 10.1016/j.wear.2019.03.016.

[8] M. Naveed, H. Schlag, F. König, and S. Weiß, "Influence of the Erodent Shape on the Erosion Behavior of Ductile and Brittle Materials," *Tribol Lett*, vol. 65, no. 1, p. 18, Mar. 2017, doi: 10.1007/s11249-016-0800-x.

[9] Y.-F. Wang and Z.-G. Yang, "Finite element model of erosive wear on ductile and brittle materials," *Wear*, vol. 265, no. 5–6, pp. 871–878, Aug. 2008, doi: 10.1016/j.wear.2008.01.014.

[10] J. G. A. Bitter, "A study of erosion phenomena," *Wear*, vol. 6, no. 3, pp. 169–190, May 1963, doi: 10.1016/0043-1648(63)90073-5.

[11] H. Wensink and M. C. Elwenspoek, "A closer look at the ductile–brittle transition in solid particle erosion," *Wear*, vol. 253, no. 9–10, pp. 1035–1043, Nov. 2002, doi: 10.1016/S0043-1648(02)00223-5.

[12] I. Finnie, "Erosion of surfaces by solid particles," *Wear*, vol. 3, no. 2, pp. 87–103, Mar. 1960, doi: 10.1016/0043-1648(60)90055-7.

[13] M. Parsi, K. Najmi, F. Najafifard, S. Hassani, B. S. McLaury, and S. A. Shirazi, "A comprehensive review of solid particle erosion modeling for oil and gas wells and pipelines applications," *J Nat Gas Sci Eng*, vol. 21, pp. 850–873, Nov. 2014, doi: 10.1016/j.jngse.2014.10.001.

[14] V. Javaheri, D. Porter, and V.-T. Kuokkala, "Slurry erosion of steel – Review of tests, mechanisms and materials," *Wear*, vol. 408–409, pp. 248–273, Aug. 2018, doi: 10.1016/j.wear.2018.05.010.

[15] S. Kumar, "Estimation of Silt Erosion in Hydro Turbine." [Online]. Available: www.ijert.org

[16] Y. I. Oka and T. Yoshida, “Practical estimation of erosion damage caused by solid particle impact,” *Wear*, vol. 259, no. 1–6, pp. 102–109, Jul. 2005, doi: 10.1016/j.wear.2005.01.040.

[17] G. R. Desale, B. K. Gandhi, and S. C. Jain, “Slurry erosion of ductile materials under normal impact condition,” *Wear*, vol. 264, no. 3–4, pp. 322–330, Feb. 2008, doi: 10.1016/j.wear.2007.03.022.

[18] P. C. Okonkwo *et al.*, “Erosion Behavior of API X120 Steel: Effect of Particle Speed and Impact Angle,” *Coatings*, vol. 8, no. 10, p. 343, Sep. 2018, doi: 10.3390/coatings8100343.

[19] Md. A. Islam, T. Alam, and Z. Farhat, “Construction of erosion mechanism maps for pipeline steels,” *Tribol Int*, vol. 102, pp. 161–173, Oct. 2016, doi: 10.1016/j.triboint.2016.05.033.

[20] A. V. Levy and P. Chik, “The effects of erodent composition and shape on the erosion of steel,” *Wear*, vol. 89, no. 2, pp. 151–162, Aug. 1983, doi: 10.1016/0043-1648(83)90240-5.

[21] H. Arabnejad, S. A. Shirazi, B. S. McLaury, H. J. Subramani, and L. D. Rhyne, “The effect of erodent particle hardness on the erosion of stainless steel,” *Wear*, vol. 332–333, pp. 1098–1103, May 2015, doi: 10.1016/j.wear.2015.01.017.

[22] N. Lin, H. Arabnejad, S. A. Shirazi, B. S. McLaury, and H. Lan, “Experimental study of particle size, shape and particle flow rate on Erosion of stainless steel,” *Powder Technol*, vol. 336, pp. 70–79, Aug. 2018, doi: 10.1016/j.powtec.2018.05.039.

[23] S. S. Rajahram, T. J. Harvey, and R. J. K. Wood, “Electrochemical investigation of erosion–corrosion using a slurry pot erosion tester,” *Tribol Int*, vol. 44, no. 3, pp. 232–240, Mar. 2011, doi: 10.1016/j.triboint.2010.10.008.

[24] S. Biswas, K. Williams, and M. Jones, “Development of a constitutive model for erosion based on dissipated particle energy to predict the wear rate of ductile metals,” *Wear*, vol. 404–405, pp. 166–175, Jun. 2018, doi: 10.1016/j.wear.2018.02.021.

[25] S. Khurana and V. Goel, “Effect of jet diameter on erosion of turgo impulse turbine runner,” *Journal of Mechanical Science and Technology*, vol. 28, no. 11, pp. 4539–4546, Nov. 2014, doi: 10.1007/s12206-014-1021-6.

[26] O. Rafae Alomar, H. Maher Abd, M. M. Mohamed Salih, and F. Aziz Ali, “Performance analysis of Pelton turbine under different operating conditions: An experimental study,” *Ain Shams Engineering Journal*, vol. 13, no. 4, p. 101684, Jun. 2022, doi: 10.1016/j.asej.2021.101684.

[27] A. K. Rai, A. Kumar, and T. Staubli, “DEVELOPING A TEST RIG TO MEASURE HYDRO-ABRASIVE EROSION IN PELTON TURBINE,” 2015. [Online]. Available: https://www.researchgate.net/publication/282691482

[28] N. Arora, A. Kumar, and S. Kumar Singal, “Technological advancement in measurements of suspended sediment and hydraulic turbine erosion,” *Measurement*, vol. 190, p. 110700, Feb. 2022, doi: 10.1016/j.measurement.2022.110700.

[29] O. Abdelaal, M. Heshmat, and Y. Abdelrhman, “Experimental investigation on the effect of water-silica slurry impacts on 3D-Printed polylactic acid,” *Tribol Int*, vol. 151, Nov. 2020, doi: 10.1016/j.triboint.2020.106410.

[30] J. A. F. O. Correia, M. S. Parancheerivilakkathil, S. Parapurath, S. Ainane, Y. F. Yap, and P. Rostron, "Flow Velocity and Sand Loading Effect on Erosion-Corrosion during Liquid-Solid Impingement on Mild Steel," 2022, doi: 10.3390/app.

[31] R. Singh Sidhu, G. Singh, and H. S. Gill, "Evaluation of the anti-erosion performance of PLA and ABS materials with two different micro textures," *Pigment and Resin Technology*, 2023, doi: 10.1108/PRT-10-2022-0127.

[32] J. Chen, Y. Wang, X. Li, R. He, S. Han, and Y. Chen, "Erosion prediction of liquid-particle two-phase flow in pipeline elbows via CFD–DEM coupling method," *Powder Technol*, vol. 275, pp. 182–187, May 2015, doi: 10.1016/j.powtec.2014.12.057.

[33] W. Peng and X. Cao, "Numerical simulation of solid particle erosion in pipe bends for liquid–solid flow," *Powder Technol*, vol. 294, pp. 266–279, Jun. 2016, doi: 10.1016/j.powtec.2016.02.030.

[34] F. Xiao *et al.*, "Numerical investigation of elbow erosion in the conveying of dry and wet particles," *Powder Technol*, vol. 393, pp. 265–279, Nov. 2021, doi: 10.1016/j.powtec.2021.07.080.

[35] L. Xu, Q. Zhang, J. Zheng, and Y. Zhao, "Numerical prediction of erosion in elbow based on CFD-DEM simulation," *Powder Technol*, vol. 302, pp. 236–246, Nov. 2016, doi: 10.1016/j.powtec.2016.08.050.

[36] R. E. Vieira, A. Mansouri, B. S. McLaury, and S. A. Shirazi, "Experimental and computational study of erosion in elbows due to sand particles in air flow," *Powder Technol*, vol. 288, pp. 339–353, Jan. 2016, doi: 10.1016/j.powtec.2015.11.028.

[37] L. Thakur and N. Arora, "A comparative study on slurry and dry erosion behaviour of HVOF sprayed WC–CoCr coatings," *Wear*, vol. 303, no. 1–2, pp. 405–411, Jun. 2013, doi: 10.1016/j.wear.2013.03.028.

[38] H. H. Tian, G. R. Addie, and E. P. Barsh, "A new impact erosion testing setup through Coriolis approach," *Wear*, vol. 263, no. 1–6, pp. 289–294, Sep. 2007, doi: 10.1016/j.wear.2007.01.090.

[39] M. Lindgren and J. Perolainen, "Slurry pot investigation of the influence of erodent characteristics on the erosion resistance of austenitic and duplex stainless steel grades," *Wear*, vol. 319, no. 1–2, pp. 38–48, Nov. 2014, doi: 10.1016/j.wear.2014.07.006.

[40] L. C. Jones, "Low angle scouring erosion behaviour of elastomeric materials," *Wear*, vol. 271, no. 9–10, pp. 1411–1417, Jul. 2011, doi: 10.1016/j.wear.2010.12.057.

[41] J. Mogan *et al.*, "Fused Deposition Modelling of Polymer Composite: A Progress," *Polymers (Basel)*, vol. 15, no. 1, p. 28, Dec. 2022, doi: 10.3390/polym15010028.

[42] S. S. Rajahram, T. J. Harvey, and R. J. K. Wood, "Electrochemical investigation of erosion-corrosion using a slurry pot erosion tester," *Tribol Int*, vol. 44, no. 3, pp. 232–240, Mar. 2011, doi: 10.1016/j.triboint.2010.10.008.

[43] N. Arora, A. Kumar, and S. Kumar Singal, "Technological advancement in measurements of suspended sediment and hydraulic turbine erosion," *Measurement*, vol. 190, p. 110700, Feb. 2022, doi: 10.1016/J.MEASUREMENT.2022.110700.

[44] R. Singh Sidhu, G. Singh, and H. S. Gill, “Evaluation of the anti-erosion performance of PLA and ABS materials with two different micro textures,” *Pigment & Resin Technology*, Feb. 2023, doi: 10.1108/PRT-10-2022-0127.

[45] I. Durgun and R. Ertan, “Experimental investigation of FDM process for improvement of mechanical properties and production cost,” *Rapid Prototyp J*, vol. 20, no. 3, pp. 228–235, Apr. 2014, doi: 10.1108/RPJ-10-2012-0091.

[46] S. Veličković, B. Stojanović, M. Babić, and I. Bobić, “Optimization of tribological properties of aluminum hybrid composites using Taguchi design,” *J Compos Mater*, vol. 51, no. 17, pp. 2505–2515, Jul. 2017, doi: 10.1177/0021998316672294.

[47] B. Stojanovic, J. Blagojevic, M. Babic, S. Velickovic, and S. Miladinovic, “Optimization of hybrid aluminum composites wear using Taguchi method and artificial neural network,” *Industrial Lubrication and Tribology*, vol. 69, no. 6, pp. 1005–1015, Nov. 2017, doi: 10.1108/ILT-02-2017-0043.

[48] S. S. Mahapatra, A. Patnaik, and A. Satapathy, “Taguchi method applied to parametric appraisal of erosion behavior of GF-reinforced polyester composites,” *Wear*, vol. 265, no. 1–2, pp. 214–222, Jun. 2008, doi: 10.1016/j.wear.2007.10.001.

[49] A. H. Bademlioglu, A. S. Canbolat, N. Yamankaradeniz, and O. Kaynakli, “Investigation of parameters affecting Organic Rankine Cycle efficiency by using Taguchi and ANOVA methods,” *Appl Therm Eng*, vol. 145, pp. 221–228, Dec. 2018, doi: 10.1016/j.applthermaleng.2018.09.032.

[50] K. Palanikumar, “Experimental investigation and optimisation in drilling of GFRP composites,” *Measurement*, vol. 44, no. 10, pp. 2138–2148, Dec. 2011, doi: 10.1016/j.measurement.2011.07.023.

[51] A. Soni, R. M. Patel, K. Kumar, and K. Pareek, “Optimization for maximum extraction of solder from waste PCBs through grey relational analysis and Taguchi technique,” *Miner Eng*, vol. 175, p. 107294, Jan. 2022, doi: 10.1016/j.mineng.2021.107294.

[52] W. H. Yang and Y. S. Tarng, “Design optimization of cutting parameters for turning operations based on the Taguchi method,” *J Mater Process Technol*, vol. 84, no. 1–3, pp. 122–129, Dec. 1998, doi: 10.1016/S0924-0136(98)00079-X.

[53] W. H. Yang and Y. S. Tarng, “Design optimization of cutting parameters for turning operations based on the Taguchi method,” 1998.

[54] C. Vidal, V. Infante, P. Peças, and P. Vilaça, “Application of Taguchi Method in the Optimization of Friction Stir Welding Parameters of an Aeronautic Aluminium Alloy,” *International Journal of Advanced Materials Manufacturing and Characterization*, vol. 3, no. 1, pp. 21–26, Mar. 2013, doi: 10.11127/ijammc.2013.02.005.

[55] C. Vidal, V. Infante, P. Peças, and P. Vilaça, “Application of Taguchi Method in the Optimization of Friction Stir Welding Parameters of an Aeronautic Aluminium Alloy,” *International Journal of Advanced Materials Manufacturing and Characterization*, vol. 3, no. 1, pp. 21–26, Mar. 2013, doi: 10.11127/ijammc.2013.02.005.

[56] B. Keshtegar, M. F. Allawi, H. A. Afan, and A. El-Shafie, “Optimized River Stream-Flow Forecasting Model Utilizing High-Order Response Surface Method,” *Water Resources Management*, vol. 30, no. 11, pp. 3899–3914, Sep. 2016, doi: 10.1007/s11269-016-1397-4.

[57] M. A. Bezerra, R. E. Santelli, E. P. Oliveira, L. S. Villar, and L. A. Escaleira, “Response surface methodology (RSM) as a tool for optimization in analytical chemistry,” *Talanta*, vol. 76, no. 5, pp. 965–977, Sep. 2008, doi: 10.1016/j.talanta.2008.05.019.

[58] D. K. Goyal, H. Singh, and H. Kumar, “An overview of slurry erosion control by the application of high velocity oxy fuel sprayed coatings,” *Proceedings of the Institution of Mechanical Engineers, Part J: Journal of Engineering Tribology*, vol. 225, no. 11, pp. 1092–1105, Nov. 2011, doi: 10.1177/1350650111412443.

[59] A. Suresh, A. P. Harsha, and M. K. Ghosh, “Solid particle erosion studies on polyphenylene sulfide composites and prediction on erosion data using artificial neural networks,” *Wear*, vol. 266, no. 1–2, pp. 184–193, Jan. 2009, doi: 10.1016/j.wear.2008.06.008.

[60] M. Lay, N. L. N. Thajudin, Z. A. A. Hamid, A. Rusli, M. K. Abdullah, and R. K. Shuib, “Comparison of physical and mechanical properties of PLA, ABS and nylon 6 fabricated using fused deposition modeling and injection molding,” *Compos B Eng*, vol. 176, p. 107341, Nov. 2019, doi: 10.1016/j.compositesb.2019.107341.

[61] T. Alomayri, H. Assaedi, F. U. A. Shaikh, and I. M. Low, “Effect of water absorption on the mechanical properties of cotton fabric-reinforced geopolymer composites,” *Journal of Asian Ceramic Societies*, vol. 2, no. 3, pp. 223–230, Sep. 2014, doi: 10.1016/j.jascer.2014.05.005.

[62] A. Suresh, A. P. Harsha, and M. K. Ghosh, “Solid particle erosion studies on polyphenylene sulfide composites and prediction on erosion data using artificial neural networks,” *Wear*, vol. 266, no. 1–2, pp. 184–193, Jan. 2009, doi: 10.1016/j.wear.2008.06.008.

[63] A. P. Harsha and A. A. Thakre, “Investigation on solid particle erosion behaviour of polyetherimide and its composites,” *Wear*, vol. 262, no. 7–8, pp. 807–818, Mar. 2007, doi: 10.1016/j.wear.2006.08.012.

[64] M. Lay, N. L. N. Thajudin, Z. A. A. Hamid, A. Rusli, M. K. Abdullah, and R. K. Shuib, “Comparison of physical and mechanical properties of PLA, ABS and nylon 6 fabricated using fused deposition modeling and injection molding,” *Compos B Eng*, vol. 176, p. 107341, Nov. 2019, doi: 10.1016/j.compositesb.2019.107341.

[65] R. Khan, M. Wieczorowski, A.-H. I. Mourad, A. H. Seikh, and T. Ahmed, “Evaluation of erosion of AISI 1045 carbon steel due to non-cohesive microparticles,” *Journal of Materials Research and Technology*, vol. 28, pp. 1423–1432, Jan. 2024, doi: 10.1016/j.jmrt.2023.12.090.

[66] J. Liu *et al.*, “Cracking and erosion behaviors of sand–clay mixtures stabilized with microbial biopolymer and palm fiber,” *Science of the Total Environment*, vol. 905, Dec. 2023, doi: 10.1016/j.scitotenv.2023.166991.